Journal of Non-Crystalline Solids 682 (2026) 124095

Contents lists available at ScienceDirect

Journal of Non-Crystalline Solids

journal homepage: www.elsevier.com/locate/jnoncrysol

Mechanisms of progressive degradation in ion-exchanged boroaluminosilicate glass: A comparative study

Seyed Ali Delbari, Lucas A. Hof *

Department of Mechanical Engineering, École de technologie supérieure, 1100 Notre-Dame Ouest, Montréal, Québec H3C 1K3, Canada

ARTICLE INFO

Keywords:
Boroaluminosilicate glass
Chemical strengthened glass, Gorilla glass,
Accelerated weathering, Degradation

ABSTRACT

While the environmental durability of chemically strengthened alkali-boroaluminosilicate glass is paramount for consumer electronics, the mechanistic coupling between residual ion-exchange stress profiles and surface weathering kinetics remains poorly defined. This study presents a comparative analysis of the degradation mechanisms in ion-exchanged Corning® Gorilla® Glass 3 (I-GG3) and its native precursor (N-GG3) subjected to accelerated weathering protocols. N-GG3 follows a gel densification model, characterized by spontaneous repolymerization and syneresis during dry cycles, processes catalyzed by the hydrolytic stability of the residual aluminosilicate network. The volumetric shrinkage associated with this densification, constrained by the underlying bulk substrate, generates localized tensile stress fields that drive stochastic pitting. Conversely, I-GG3 undergoes network depolymerization driven by the thermodynamic instability and high chemical potential of the potassium-enriched surface. Rapid alkali leaching triggers a localized alkaline attack that selectively depletes intermediate network formers (Al, Mg), inhibiting densification and yielding a porous hydrogel layer. Despite the formation of this hydrated layer, the residual compressive stress profile suppresses vertical crack propagation, promoting a uniform dissolution regime that preserves optical transmission and bulk damage tolerance.

1. Introduction

Alkali aluminosilicate glasses are widely used as high-strength cover glasses in consumer electronics such as smartphones [1–3]. The combination of SiO_2, Al_2O_3, and alkali metal oxides leverages these glasses with high mechanical strength and chemical stability [4,5]. Moreover, mechanical properties of silicate glass networks are modified by the addition of Al_2O_3 since it affects network rigidity and Non-Bridging Oxygen (NBO) concentration. The presence of NBOs disrupts the continuity of the glass network, thereby influencing corrosion resistance and crack initiation behavior [6,7]. The structural role of aluminum (Al) and the Al/alkali ratio dictate NBO formation. NBOs typically form when the Al/alkali ratio is less than one, a prerequisite for ion-exchange treatment [4,8]. As boron oxide serves a multifaceted role in aluminosilicates, it is frequently incorporated into the glass matrix to provide property combinations that would otherwise be technically difficult to achieve [9,10]. Boron acts as a flux for reducing melting temperatures and inhibiting devitrification. It is also essential to lower the Coefficient of Thermal Expansion (CTE) and to enhance the thermal shock resistance [11,12]. Boron incorporation, primarily occurring as rigid, four-coordinated tetrahedral units ($[BO_4]$) improves network connectivity and mechanical performance. A higher fraction of stable $[BO_4]$ units relative to trigonal $[BO_3]$ units correlates with increased microhardness and chemical durability against aqueous and acidic corrosion [9,13,14].

These alkali aluminosilicate glasses commonly undergo an ion exchange process to achieve the high mechanical strength necessary for applications including smartphones, wearables, and automotive displays [15–18]. In this process, typically smaller Na^+ ions (ionic radius ≈ 1.02–1.18 Å) from the submerged glass in a molten KNO_3 salt bath are replaced by larger K^+ ions (ionic radius ≈ 1.38–1.51 Å) [19–21]. The resulting lattice dilation creates a surface compressive stress layer, enhancing flexural strength and crack propagation resistance [22–25].

Furthermore, complex mixed-ion interactions are caused by the presence of both Na^+ and K^+ in this layer. Unlike the classical Mixed Alkali Effect (MAE) in melt-formed glasses, the ion-exchange process generates a distinct mixed-alkali blocking effect because it occurs below the glass transition temperature (T_g) [26,27]. Consequently, the resultant layer acts as a stuffed derivative of the parent glass where larger K^+ ions are forced into smaller sites previously occupied by Na^+ ions [28].

* Corresponding author.
E-mail address: lucas.hof@etsmtl.ca (L.A. Hof).

https://doi.org/10.1016/j.jnoncrysol.2026.124095
Received 11 December 2025; Received in revised form 30 March 2026; Accepted 31 March 2026
Available online 3 April 2026

This steric hindrance restricts K^+ diffusion, significantly reducing its mobility compared to the original sodium ions [27]. Chemical durability of the strengthened layer is significantly altered by this modified structural state compared to single-alkali-based glass [29]. Therefore, to isolate the effects of chemical strengthening, a comparative analysis between the ion-exchanged glass and its native precursor is necessary to understand its degradation behavior under weathering.

For simulating these real-world weathering conditions, a protocol adapted from the ASTM G155 standard was applied in this study, wherein the glass was subjected to cyclic exposure of moisture, heat, and specifically filtered UV radiation. UV radiation was included as it acts as an accelerating stressor [30,31]. While 340 nm photons (~3.65 eV) cannot directly cleave intrinsic Si-O bonds (~4.8 eV), they effectively interact with trace impurities inherent to the glass matrix [31–33]. Iron impurities (Fe^{2+}/ Fe^{3+}) act as electron traps that undergo photoionization to form color centers (solarization) [34,35], while Tin (Sn^{2+}/ Sn^{4+}), present as a fining (bubble removal) agent, possesses a strong UV absorption cross-section that can catalyze localized structural instability [34]. Weathering is therefore a combined attack where UV-induced defects, mediated by trace Fe and Sn species, facilitate the degradation of the strengthened layer [30,34].

Although numerous studies have independently investigated the principles of ion-exchange strengthening [16,36] and the general mechanisms of glass corrosion [37–39], a significant gap remains regarding how these mechanisms interact over time. Previously, the effect of weathering on strengthened glass for fixed durations [29] and degradation in standard soda-lime-silica glasses [40] was assessed; however, there is a notable absence of systematic, time-dependent comparative analyses for high-performance boroaluminosilicates. Therefore, this gap is addressed by directly monitoring the progressive degradation of a commercial Chemically Strengthened Glass (CSG), specifically Corning® Gorilla® Glass 3 (referred to herein as I-GG3), alongside its native precursor (referred to as N-GG3) under accelerated weathering conditions adapted from the ASTM G155 standard. This work utilizes molecular-level evidence via Fourier Transform Infrared spectroscopy (FTIR) and micro-Raman spectroscopy to decode the distinct network responses. The results indicate that ion-exchange is not merely mechanical shielding; it induces structural re-speciation, particularly within the borate network, creating a chemically distinct surface layer. This modified layer changes the thermodynamic and kinetic pathways, acting as a robust barrier against hydrolytic leaching. By correlating these structural shifts with changes in optical transmittance and mechanical properties, this study offers insights critical for lifespan prediction and circular economy strategies. The framework of this study is illustrated in Fig. 1.

2. Materials and methods

The experimental workflow, including sample preparation, accelerated weathering, cleaning, and characterization, is outlined in Fig. 2.

2.1. Materials

Two series of glass were examined. The primary material was commercially available CSG, specifically I-GG3, purchased from Abrisa Technologies, USA. The as-received I-GG3 samples had dimensions of 25 mm × 25 mm × 0.55 mm. Key properties of the as-received I-GG3 are detailed in Table 1. The second material was the native precursor (N-

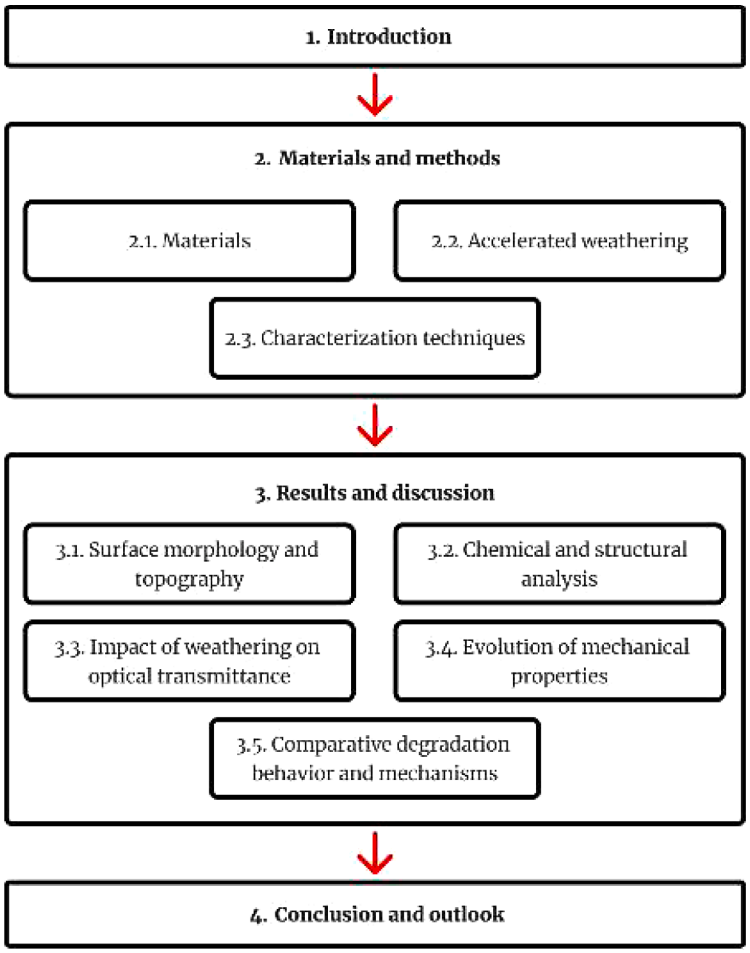

Fig. 1. Schematic representation depicting the framework of the current study.

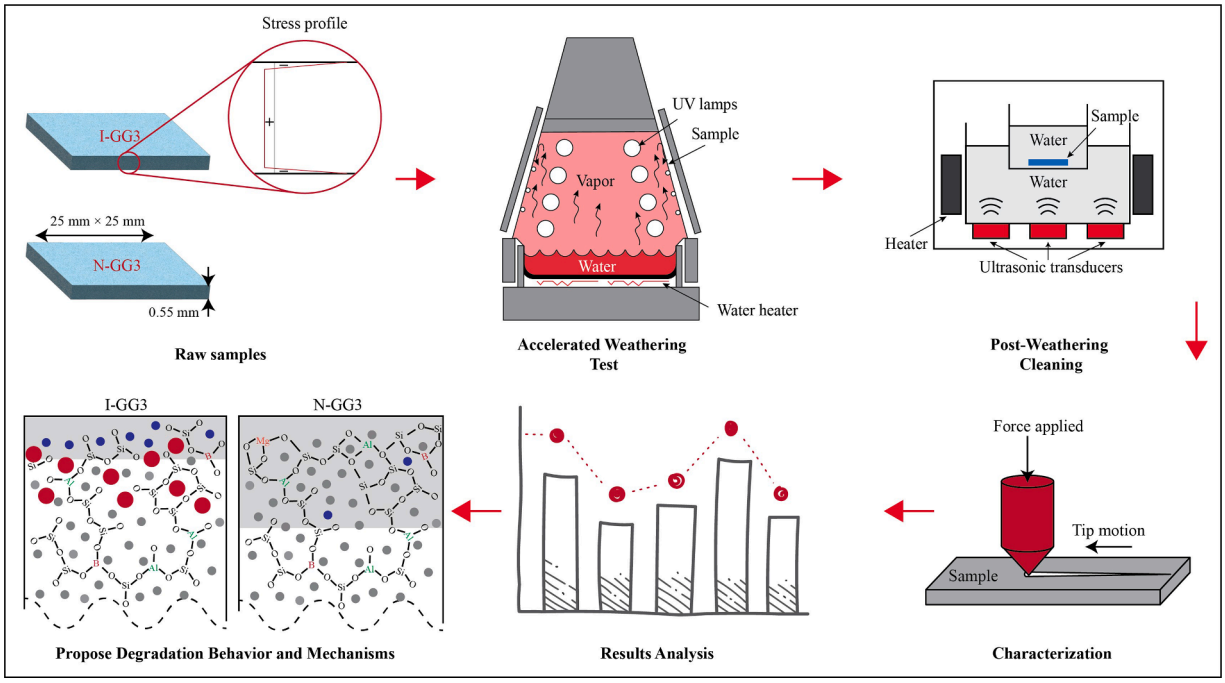

Fig. 2. Schematic representation of the experimental workflow implemented in this study.

Table 1
Key properties of the as-purchased Corning® GG3. Values are sourced from the Corning® datasheet [42] with stress-related parameters (*) measured by the supplier, Abrisa Technologies.

Dimensions	25 mm × 25 mm × 0.55 mm
Density	2.39 g/cm^3
Young's Modulus	70 GPa
Poisson's Ratio	0.22
Shear Modulus	28.5 GPa
Vickers Hardness (200 g load), Strengthened	653 kgf/mm^2
Fracture Toughness	0.66 MPa m$^{0.5}$
Coefficient of Thermal Expansion (0–300°C)	75.8 × 10^{-7}/°C
Compressive Stress *	780.6 ± 1.4 MPa
Depth of layer *	43.8 ± 3.1 μm

* Compressive stress and depth of layer values were measured by Abrisa Technologies using a commercial FSM-6000LE surface stress meter.

GG3) used for comparative purposes. The specific nominal composition of N-GG3 and the role of each constituent in the structure have been summarized in Table 2.

The I-GG3 samples were purchased in a chemically strengthened state. According to the manufacturer's patent specifications for Corning® Gorilla® Glass Code 2320 [41], the strengthening process consisted of immersion in a molten KNO_3 salt bath at 420°C for 5.5 h. As illustrated in Fig. 3 (reproduced from [41]), the resulting potassium concentration profile, characterized by electron microprobe analysis,

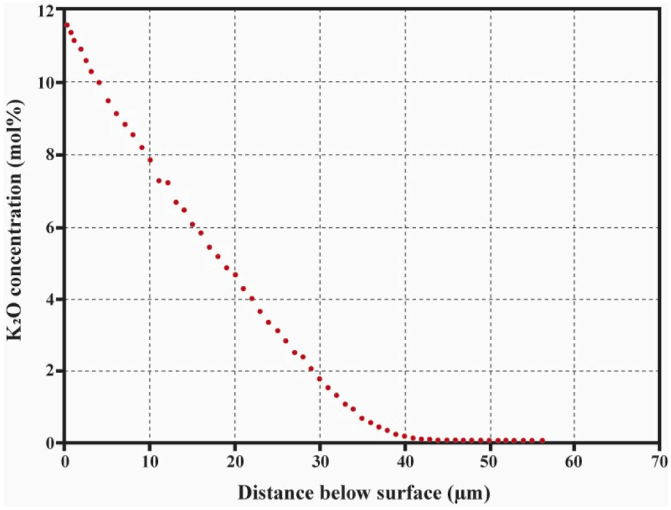

Fig. 3. K_2O concentration profile of I-GG3 showing the surface concentration of ~12 mol %. Reproduced from [41].

effectively raises the surface K_2O concentration to approximately 12 mol % [41].

Table 2
Detailed composition, structural roles, and functional properties of oxides in the as-received N-GG3 glass.

Oxide	Mol %	Structural location	Coordination	Dominant bond type	Primary functional role	Ref.
SiO_2	67.55	Network former	Tetrahedral	Covalent	Skeleton / Connectivity	[41,43,44]
Na_2O	13.66	Modifier	Interstitial	Ionic	Charge compensation / Flux	[41,44]
Al_2O_3	12.67	Network former	Tetrahedral	Ionocovalent	Rigidity / Corrosion Resistance	[41,45]
B_2O_3	3.67	Network Former	Tetrahedral [BO_4]	Covalent	Hardness / CTE reduction	[41,44]
MgO	2.33	Modifier / Intermediate	Octahedral	Ionic	Network stiffener	[41,46]
SnO_2	0.10	Fining agent	Octahedral	Ionocovalent	Bubble removal	[41,47,48]
K_2O	0.014	Modifier	Interstitial	Ionic	Enhances ion-exchange kinetics	[27,41,44]
Fe_2O_3	0.008	Impurity	Tetrahedral	Ionocovalent	Color center (solarization)	[41,49,50]
ZrO_2	0.005	Intermediate	Octahedral	Ionocovalent	Durability enhancer	[41,48,51]

2.2. Accelerated weathering

In accordance with protocols adapted from ASTM G155, N-GG3 and I-GG3 samples were subjected to accelerated weathering tests using a Q-SUN Xe-3 xenon arc test chamber (Q-Lab Corporation, USA). Three samples were analyzed per condition. The protocol used 2-h cycles (Black Panel Temp: 63°C, Air Temp: 48°C, RH: 30 %). The cycle included a UV light exposure phase (0.35 W/m^2 at 340 nm, 1 h 42 min) followed by a phase of UV light exposure combined with water spray (18 min). To examine the progressive degradation, samples were exposed for 3, 6, 12, and 24 days. This geometric sequence captures both initial degradation kinetics and long-term saturation. Pristine samples of both N-GG3 and I-GG3 were kept as controls. Following the weathering period, samples were cleaned by immersion in an ultrasonic bath with deionized water at 60°C for 60 min. Prior to characterization, they were wiped with cleanroom wipers (Kimwipes Low-Lint) and rinsed with ethanol. This cleaning procedure removed loosely adhered precipitates, ensuring analysis focused on persistent weathering by-products and the glass surface.

2.3. Characterization techniques

Experiments were conducted in a specific sequence where non-destructive optical and morphological characterizations were conducted prior to destructive mechanical testing. Destructive tests (indentation/scratch) were spatially separated to prevent interference.

2.3.1. Surface morphology and topography

Surface morphology evolution was assessed using an Olympus LEXT OLS4100 confocal laser scanning microscope to generate 3D topography maps and quantify roughness parameters, specifically arithmetic mean height (S_a) and root mean square height (S_q). 14 images were randomly sampled over a broad surface area to capture the full range of material heterogeneity. Post-acquisition, all topographic images were analyzed using Gwyddion software (Ver. 2.68, Czech Metrology Institute, Czech Republic). To isolate the relevant roughness data, the following processing steps were applied: (1) Level data by mean plane subtraction to correct sample tilt; (2) Polynomial background removal to remove form and waviness (long-wavelength cutoff); and (3) Interpolation of small defects to remove non-native high-frequency artifacts (short-wavelength cutoff), such as dust or external particles, ensuring the analysis focused solely on the glass surface texture.

2.3.2. Chemical and structural analysis

Elemental depth profiles, particularly for Na^+ and K^+, were acquired using Time-of-Flight Secondary Ion Mass Spectrometry (ToF-SIMS). An ION-TOF IV ToF-SIMS spectrometer was used in this test and spectra were measured using a Bi^+ primary ion beam with a mass resolution (M/ΔM) of ≥ 8000. Depth profiles were obtained by sputtering with an O^{2+} keV beam over a 1000 μm × 1000 μm sputter area. The actual analysis area for monitoring positive secondary ions was restricted to the sputtered crater (200 μm × 200 μm) with 128 × 128-pixel resolution, under a beam voltage of 25 kV and a pulsed beam current of 1.1 pA in bunch mode (pulse width of 19.9 ns).

To enable quantitative comparison and mitigate matrix effects, raw secondary ion intensities (I_i) were normalized using a double-normalization procedure. Matrix correction involved normalizing the intensity of mobile ions (I_i, e.g., Na^+ and K^+) to the intensity of a stable structural reference element. Since Si^+ acts as the primary network former, it was selected as the reference (I_{Si+}) for this silicate glass composition, yielding the ratio $R_i = I_i / I_{Si+}$. Subsequently, the relative concentration (C / C_0) was calculated. Normalization of ratio R_i obtained from the weathered samples was performed by using the corresponding average ratio measured in the pristine glass ($R_{i,p}$). The final metric represents elemental change relative to the initial composition:

$$C/C_0 = R_i/R_{i,p} \quad (1)$$

For visualization of elemental depletion (C / C_0 < 1) and enrichment (C / C_0 > 1), depth profiles were plotted as C / C_0 versus sputter time.

Surface morphology and elemental composition of corrosion products were analyzed using a Hitachi SU-8230 Field Emission Scanning Electron Microscope (FESEM) in conjunction with Energy Dispersive X-Ray Spectroscopy (EDS) after 24 days of weathering. While FESEM micrographs provided visual information of degraded surface, EDS elemental maps were used to determine the corrosion products composition (accelerating voltage of 5 kV). Surface structural changes were characterized using FTIR and micro-Raman spectroscopy. FTIR reflectance spectra were recorded with FTIR spectrometer (PerkinElmer Spectrum Two) operating in reflectance mode (R). These reflectance spectra were mathematically converted to absorbance units (-log(R)) before deconvolution, and subsequently normalized for comparison. To track changes in the silicate network (Si-O-Si/Si-O-Al) and the borate speciation (BO_3/BO_4), spectra were recorded in the 550–1600 cm^{-1} range. Additionally, micro-Raman spectra were acquired using a WITec Alpha 300 confocal Raman spectrometer (532 nm continuous-wave laser, 60 mW, fiber-coupled). The data collected (0–1300 cm^{-1} Raman shift range) focused on the network vibrational modes pertinent to silicate and boroaluminosilicate structures. MagicPlot Pro software (Ver. 3.0.1, Magicplot Systems, Russia) was utilized for the deconvolution of both FTIR and micro-Raman, thereby enabling the examination of overlapping peaks and structural alterations. For all spectroscopic analyses, three tests were performed for each condition, and values are reported as the average ± standard deviation.

2.3.3. Optical transmittance

Optical transmittance spectra were measured using a PerkinElmer UV–Vis spectrophotometer over a wavelength range of 200–900 nm. Transmittance (T %) is calculated as:

$$T\% = (I/I_0) \times 100 \quad (2)$$

where I is the intensity reaching the detector and I_0 is the incident light intensity [52]. The transmittance at 380 nm was specifically tracked to monitor degradation-induced Rayleigh scattering.

2.3.4. Mechanical properties

Surface compressive stress profiles for I-GG3 were measured using an Orihara FSM-6000LE surface stress meter [53]. Vickers microhardness (HV) was measured on N-GG3 and I-GG3 samples based on ASTM C1327 [54] using a CLEMEX JS2000 tester (500 gf load, 10 s dwell). To minimize experimental error, all indentation tests were performed consecutively on the same day at a controlled laboratory temperature of 22 ± 1°C and a relative humidity of 38 ± 2 %. Hardness was calculated using the average diagonal length (d) of eight indents:

$$HV = 1.8544 \times \left(\frac{P}{d^2}\right) \quad (3)$$

where P is the load in kgf and d is the mean diagonal in mm. Scratch resistance was assessed using an Anton Paar MCT^3 micro-scratch tester equipped with a sphero-conical diamond indenter (10 μm radius, 90° angle) where a progressive load (F_n) ranging from 50 mN to 1000 mN was applied over a 2000 μm length. Consequently, the first critical load (Lc_1), denoting the onset of failure, was reported. Estimation of Indentation Fracture Toughness (K_{IFT}) of N-GG3 samples was accomplished using the indentation fracture method [55]. Measurement of radial cracks generated by Vickers indentations (500 gf load) was performed, and the K_{IFT} (MPa m$^{1/2}$) was calculated using the equation proposed by Anstis et al. [56]:

$$K_{IFT} = 0.016 \times (E/H)^{0.5} \times \left(P/c^{1.5}\right) \quad (4)$$

where E is Young's modulus (70 GPa), H is the Vickers hardness, P is the indentation load, and c is the crack length from the center of the indent to the crack tip.

3. Results and discussion

3.1. Surface morphology and topography

When N-GG3 and I-GG3 samples were subjected to accelerated weathering, noticeable surface alterations were observed. Optical micrographs and corresponding height maps of samples weathered for 24 days, as shown in the optical micrographs (Fig. 4a, c) and height maps (Fig. 4b, d), reveal that both materials underwent significant surface degradation. While qualitative inspection showed general deterioration in both cases, quantitative roughness analysis and 3D topographic reconstructions revealed distinct durability differences of early (3-day) and late-stage (24-day) weathering (Fig. 5a). The topographic evolution from 3 days to 24 days is detailed in Fig. 5b-e. Pristine N-GG3 ($S_a \approx 17.0$ nm, $S_q \approx 26.6$ nm) and I-GG3 ($S_a \approx 17.7$ nm, $S_q \approx 28.7$ nm) showed comparable surface quality, confirming ion-exchange maintains the optical finish. However, a more severe degradation trajectory was exhibited by N-GG3. After 24 days, roughness of N-GG3 escalated significantly to $S_a \approx 37.8$ nm ($S_q \approx 98.3$ nm), whereas superior resistance was demonstrated by I-GG3, limiting roughness increases to $S_a \approx 30.3$ nm ($S_q \approx 74.4$ nm).

While S_a provides a global index of topological degradation, a fundamental shift in corrosion mechanism is signaled by a divergence in S_q standard deviations. The increase in S_q statistical dispersion for N-GG3 (from 0.7 to 15.7) indicates stochastic pitting corrosion. In stress-free silicate networks, hydrolysis preferentially attacks high-energy sites (e.g., micro-flaws), causing rapid vertical pitting rather than uniform recession [57]. This results in a surface dominated by topological outliers, accounting for substantial expansion in statistical deviation.

Conversely, a much narrower statistical distribution (standard deviations from 3.1 to 6.0 for S_q) was maintained by I-GG3 surface. This implies that degradation in strengthened glass is dominated by uniform surface recession rather than highly localized pitting. Topological data suggests that formation of deep outliers is suppressed by chemically strengthened layer, maintaining a more homogeneous surface texture despite aggressive weathering environments.

The morphological stability of I-GG3 results from the compressive stress layer inhibiting vertical crack growth. Surface micro-flaws

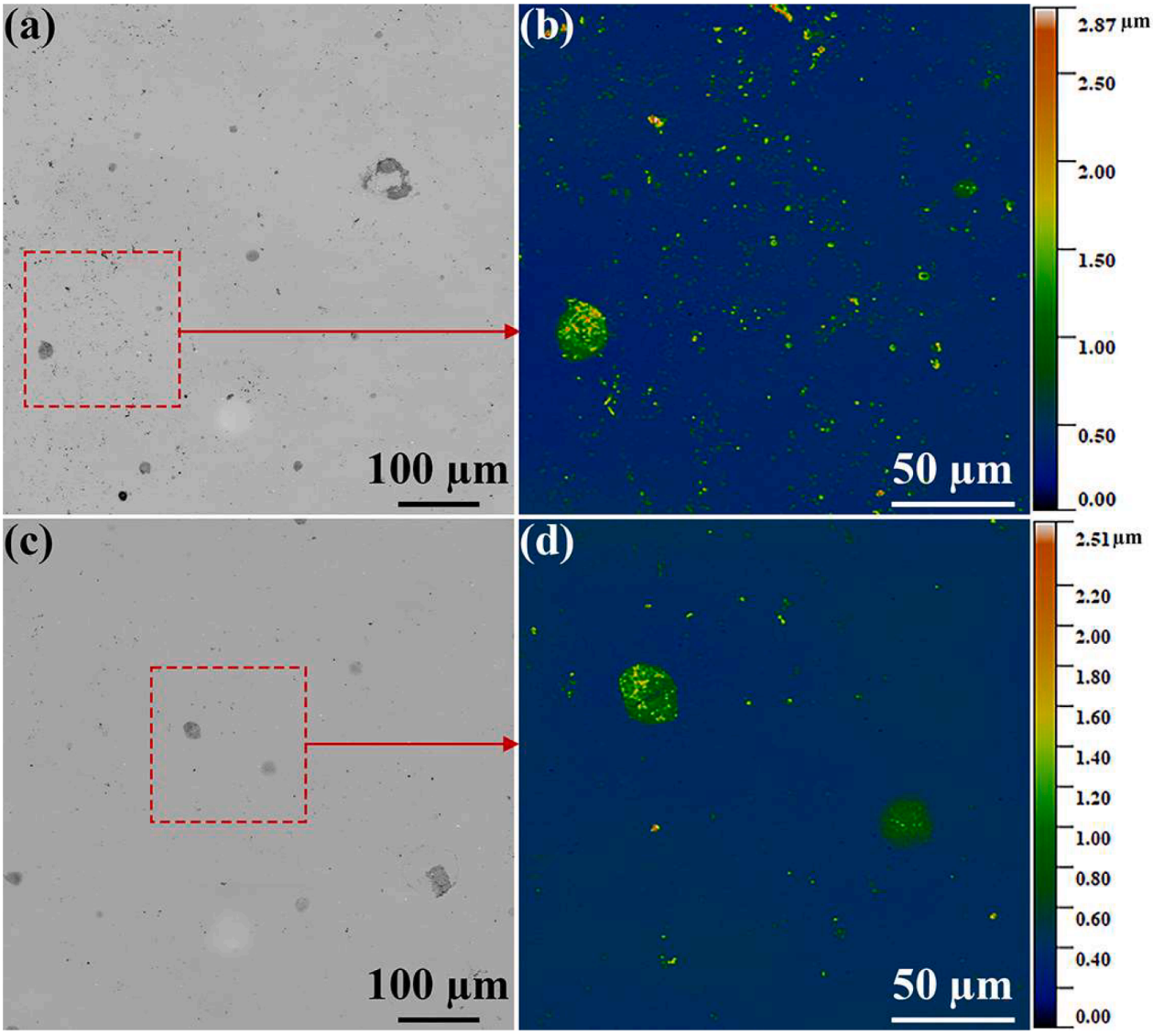

Fig. 4. Surface morphology of (a, b) N-GG3 and (c, d) I-GG3 samples after 24 days of accelerated weathering: (a, c) confocal optical micrographs and (b, d) their corresponding 2D height maps, illustrating the localized degradation.

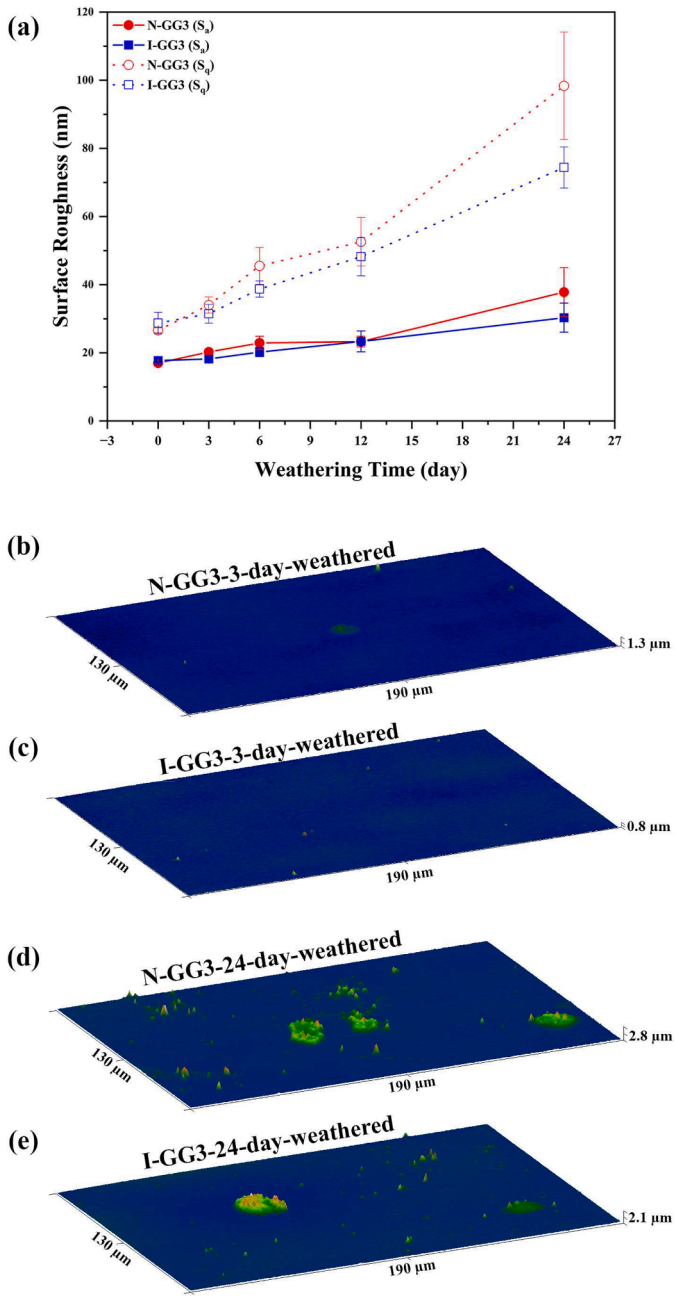

Fig. 5. (a) Quantitative analysis of surface topography including S_a and S_q values as a function of weathering time along with (b-e) the 3D topographic reconstructions comparing the surface morphologies of N-GG3 and I-GG3 after 3 and 24 days of weathering.

(Griffith flaws) are mechanically clamped by high residual compression (~780 MPa) [58]. According to stress-corrosion theory, activation energy for Si-O bond hydrolysis, which is equivalent of crack growth, is lowered by tensile stress at a crack tip [37]. In I-GG3, crack opening is opposed by the compressive field, sterically hindering access of water molecules to strained bonds at the crack tip. Instead, corrosion is forced to proceed laterally via uniform surface recession (etching), resulting in significantly lower S_q standard deviation and smoother topography observed in strengthened glass.

This topographic evolution impacts optical performance (discussed in Section 3.3). Roughness values approach the regime where short-wavelength (UV/Blue) Rayleigh scattering becomes significant. Because growth of these scattering centers is effectively limited by I-GG3 compared to N-GG3, optical transmission efficiency of display glass is preserved by the mechanical stress profile, which will be discussed more in Section 3.3.

3.2. Chemical and structural analysis

Probing of the extreme outer surface (< 1800 sputter time ≈ 150 nm) was studied by TOF-SIMS depth profiling to reveal the primary kinetic drivers of degradation. Depth profiles plotted C/C_0 versus sputter time (Fig. 6) to visualize depletion (< 1) and enrichment (> 1). The first 50–10 sputter time data were excluded in the following discussion to isolate the effect of possible surface contamination. The profiles reveal divergent leaching kinetics between native and strengthened glasses, driven by distinct reactivities and transport limitations.

N-GG3 exhibits classical diffusion-controlled leaching behavior. While Na^+ depletes monotonically, the aluminosilicate backbone remains stable, with Magnesium (Fig. 6c) and aluminum (Fig. 6d) concentrations near unity. This stability is governed by the balance between leaching kinetics and environmental dilution. In N-GG3, the intrinsic lower polarizability of the Na-NBO bonds compared to the K-NBO bond [59] results in a moderate ion-exchange rate. Consequently, the leached sodium is effectively washed away by the cyclic water spray before the concentration of hydroxyl ions in the static moisture film can accumulate to the critical threshold (pH > 9) required for network dissolution [60]. Thus, atmospheric equilibration (Eq. (5)) maintains a near-neutral pH, preserving Al-O-Si and Mg-O bonds. This preservation of the aluminosilicate backbone is critical; it retains the structural network and catalytic sites necessary to support the repolymerization (gel densification) mechanism during subsequent drying phases [61].

$$CO_2(aq) + H_2O(l) \leftrightarrow H^+(H_3O^+)(aq) + HCO_3^- \quad (5)$$

In contrast, I-GG3 exhibits significant destabilization of both mobile cations and network modifiers. The magnesium profile reveals a depletion zone where the concentration drops to ~0.25 in the near-surface region, accompanied by aluminum loss. This instability is driven by a synergistic failure mechanism. First, the larger ionic radius of K^+ (1.38–1.51 Å) increases the polarizability of the associated NBOs [59]. Second, the ion-exchange induced lattice dilation generates significant elastic strain energy [62]. While this compressive stress mechanically inhibits vertical crack propagation [29] (as detailed in Section 3.5), it acts as a mechanochemical catalyst at the molecular level, weakening the strained Si-O bonds and lowering the activation energy for hydrolysis [63].

The combination of this mechanochemical activation and the high surface concentration results in a burst release of alkali ions that overwhelms the dilution capacity of the surface moisture film. This rapid efflux causes a localized, instantaneous spike in alkalinity (pH > 9–10), transitioning the system from passive leaching to destructive network dissolution [64,65].

Simultaneously, a complex dynamic, characterized by distinctive subsurface accumulation ($C / C_0 > 1$) rather than simple monotonic depletion, is revealed by the sodium profile in I-GG3. In the strengthened layer, the larger potassium ions create a mixed-alkali blocking effect that hinders the diffusion of bulk sodium to the surface. As surface K^+ ions are rapidly stripped away by weathering, migration of Na^+ ions from the bulk upward acts to fill the resulting structural vacancies. However, their transport is kinetically impeded by the remaining mixed-cation network, causing an accumulation in the sub-surface region. This results in an unusual surface state: a layer that is chemically stripped of its intermediate network formers (Al, Mg) due to aggressive alkaline attack, yet irregularly enriched in sodium due to the diffusion barrier.

In addition, FESEM-EDS provided macroscopic assessment of the residual glass network and corrosion products. Fig. 7 presents wide-area EDS spectra after 24 days of weathering. These spectra validate the composition and identify persistent environmental residues.

The N-GG3 spectrum (Fig. 7a) confirms baseline chemistry,

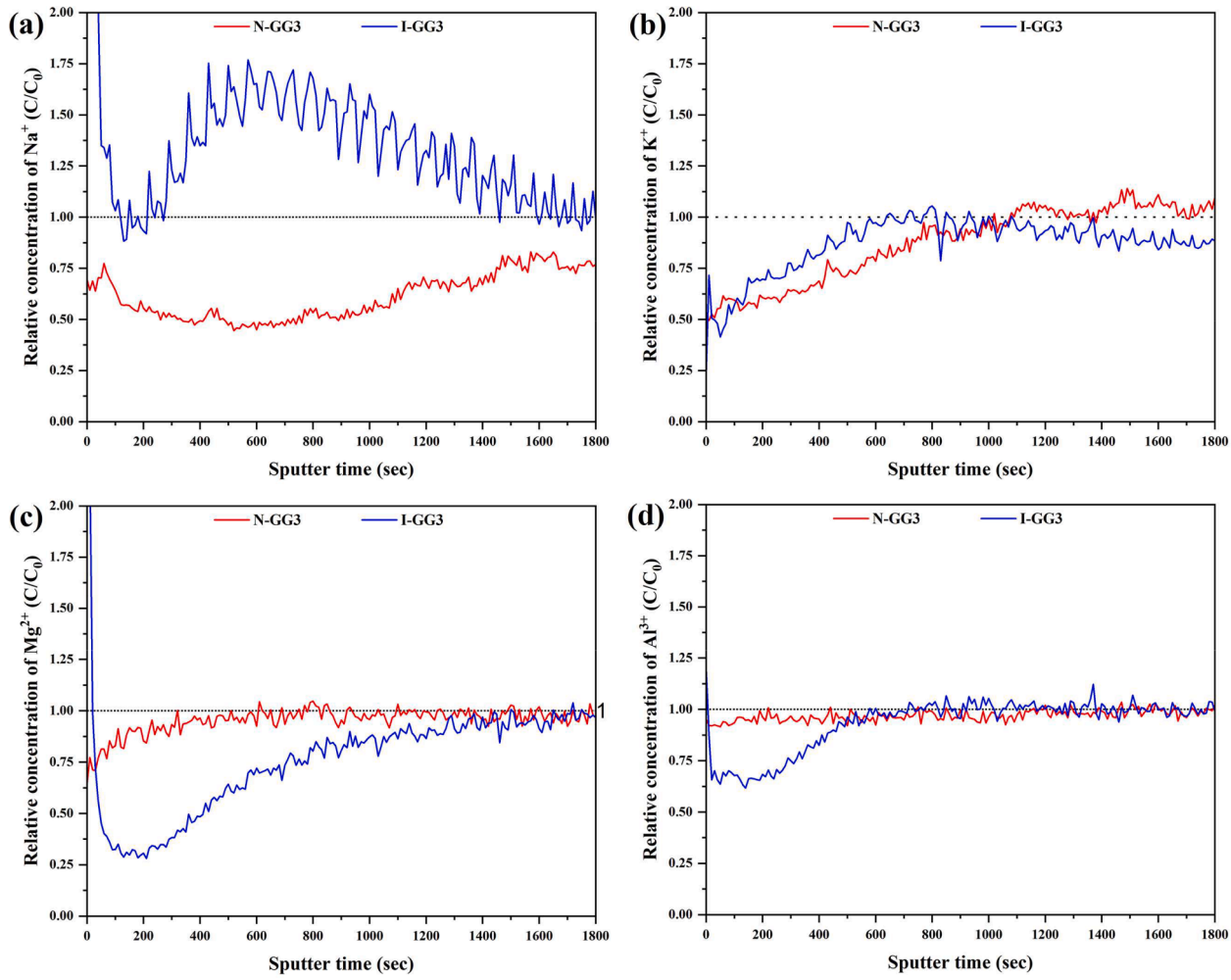

Fig. 6. TOF-SIMS depth profiles showing normalized relative concentration of (a) Na, (b) K, (c) Mg, and (d) Al ions as a function of sputter time for pristine and 24-day-weathered N-GG3 and I-GG3 samples.

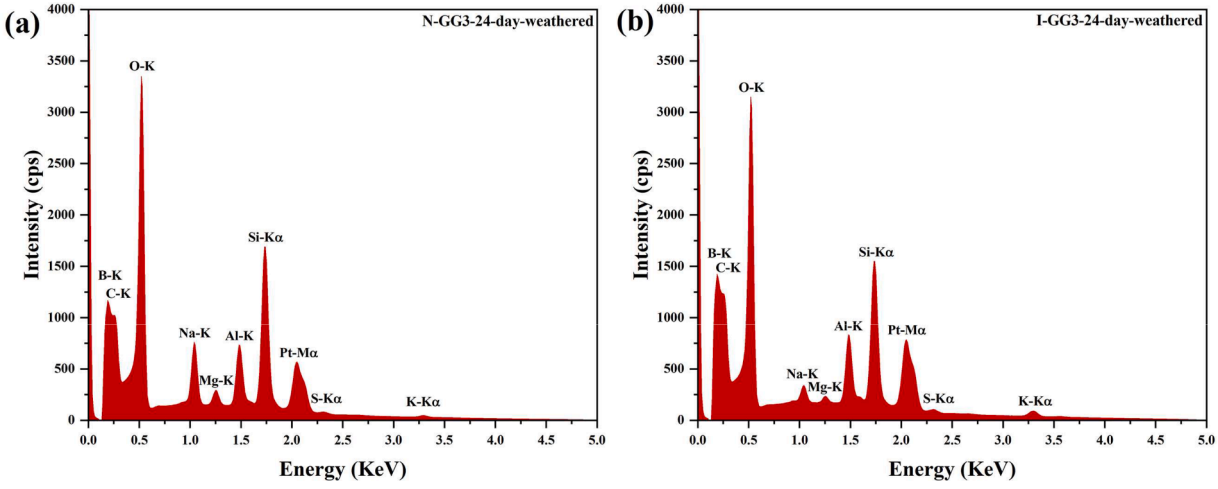

Fig. 7. EDS spectra for (a) N-GG3 and (b) I-GG3 samples after 24-day weathering.

exhibiting characteristic peaks consistent with Table 2. However, the spectrum also reveals distinct carbon and sulfur peaks, marking degradation. These persistent signals indicate entrapment of insoluble contaminants or precipitates within the porous leached layer, surviving cleaning. Additionally, compositional impact of the strengthening process is reflected by the spectrum for I-GG3 as shown in Fig. 7b, exhibiting a stronger potassium peak relative to native glass.

Spatial distribution of these species is further revealed by FESEM micrographs and elemental maps in Fig. 8. In both N-GG3 (Fig. 8a) and I-GG3 (Fig. 8b), these localized deposits manifest as silicate-based crusts.

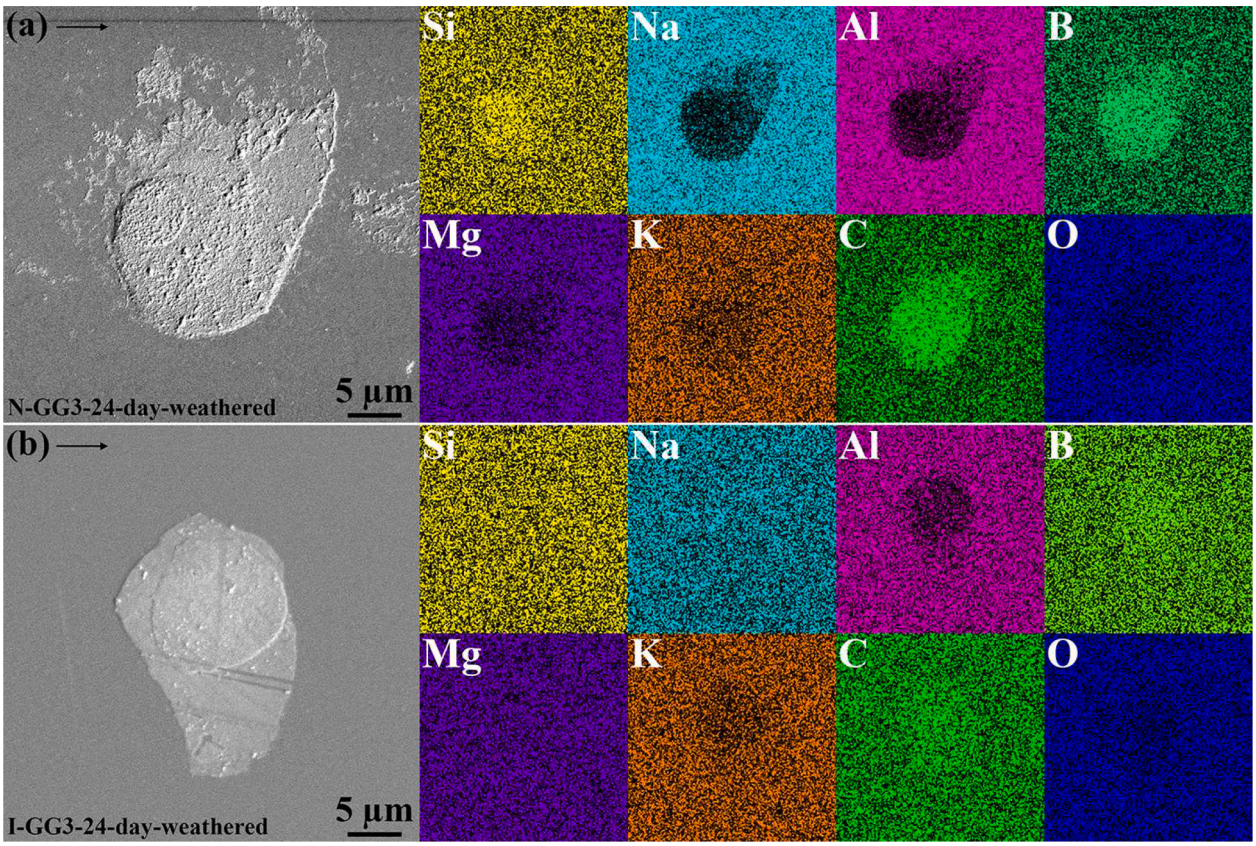

Fig. 8. FESEM micrographs and corresponding EDS elemental maps for (a) N-GG3 and (b) I-GG3 samples after 24 days of weathering.

These crusts are enriched in boron and carbon, likely from trapped carbonates or organic adsorbates.

For the N-GG3 surface, the presence of Si-enriched crusts, despite TOF-SIMS evidence of a chemically stable aluminosilicate backbone, is explained by dissolution-precipitation occurring at the extreme outer surface layer. Although the bulk network remains intact, amorphous silica possesses finite solubility (~115 ppm at 25°C) [66]. Consequently, hydrolysis of the top few nanometers of glass is caused by cyclic water spray, releasing monomeric silicic acid ($Si(OH)_4$) [67], into a surface moisture film without disrupting deeper Al/Mg profiles. In I-GG3, while the deeper network is disrupted by alkaline attack, the same phenomenon applies to the silica-rich leachate.

As surface moisture evaporates during the dry cycle (63°C), dissolved solids become supersaturated, a process driven by syneresis [68]. As the hydrated silica layer condenses, the pore water becomes enriched with dissolved silicic acid and borate species. This solution is mechanically expelled to the surface [69]. Upon evaporation, precipitation of these species as localized, insoluble borosilicate crusts observed in Fig. 8 occurs. The absence of strong alkali signals confirms that soluble salts were washed away, leaving reprecipitated framework elements.

Vibrational spectroscopy reveals a distinct structural reorganization mechanism in the ion-exchanged glass compared to the native precursor. Comparing FTIR spectra of pristine N-GG3 and I-GG3 reveals structural impacts of the ion-exchange process. The I-GG3 spectrum exhibits distinct high-frequency bands at ~1400 cm^{-1} (Band A, Fig. 9c, Table 3) and 1287 cm^{-1} (Band B, Fig. 9c, Table 3), absent in native glass. In the N-GG3 network, boron exists primarily as charge-compensated, tetrahedrally coordinated units [BO_4] [70]. During ion exchange, the introduction of larger K^+ ions and the resulting compressive stress make this compact coordination energetically unfavorable. Consequently, the network relaxes by converting tetrahedral [BO_4] into planar [BO_3] units to decrease network rigidity and provide required space for larger K^+ ions [11,13]. Crucially, persistence of these [BO_3] signatures in weathered I-GG3 samples demonstrates that the chemically strengthened surface retains a distinct, structurally modified potassium-boroaluminosilicate phase even after degradation.

Evolution of the silicate network under weathering, tracked via a dominant T-O-T asymmetric stretching mode (Band D, Fig. 9a-d, Table 3), further differentiates degradation pathways. A significant blue shift of +24.8 cm^{-1} is exhibited by N-GG3. This shift signifies chemical purification toward vitreous silica (~1100 cm^{-1} [71]), confirming that the network degrades into a simplified, polymerized silica leached layer. This behavior is consistent with the discussion in Section 3.5, indicating that in dry periods of the weathering protocol, condensation of silanols into siloxane bridges is favorable. However, volumetric polymerization shrinkage accompanies this conversion to a dense silica phase, which will be discussed in Section 3.5.

In contrast, a smaller but still significant blue shift (+17.0 cm^{-1}) is displayed by I-GG3 glass, confirming that repolymerization is a universal response to leaching; the silicate network in strengthened glass also attempts to heal via condensation. However, the outcome of this repolymerization is fundamentally different. In I-GG3, spectral variance broadens, consistent with the mixed-alkali blocking effect (TOF-SIMS). Competition between leaching K^+ and back-diffusing Na^+ creates a chemically stratified surface. The extensive depletion of intermediate network formers (Al, Mg) creates a lattice with significant vacancies. Consequently, while Si-O bonds shorten, the bulk network cannot effectively collapse into a dense solid. Instead, the surface evolves into a porous hydrogel layer. This layer represents a state where the network is chemically connected (bridged) but physically porous and water-filled, explaining the significant drop in HV despite the preservation of the underlying compressive stress profile (Section 3.4).

Analysis of the medium-range order via the Raman Boson peak (Band q) confirms the divergence between densification and hydrogel formation. In native glass, the Boson peak exhibits a positive shift (+11.0 cm^{-1}), indicating the repolymerizing silica gel has evolved into a rigid,

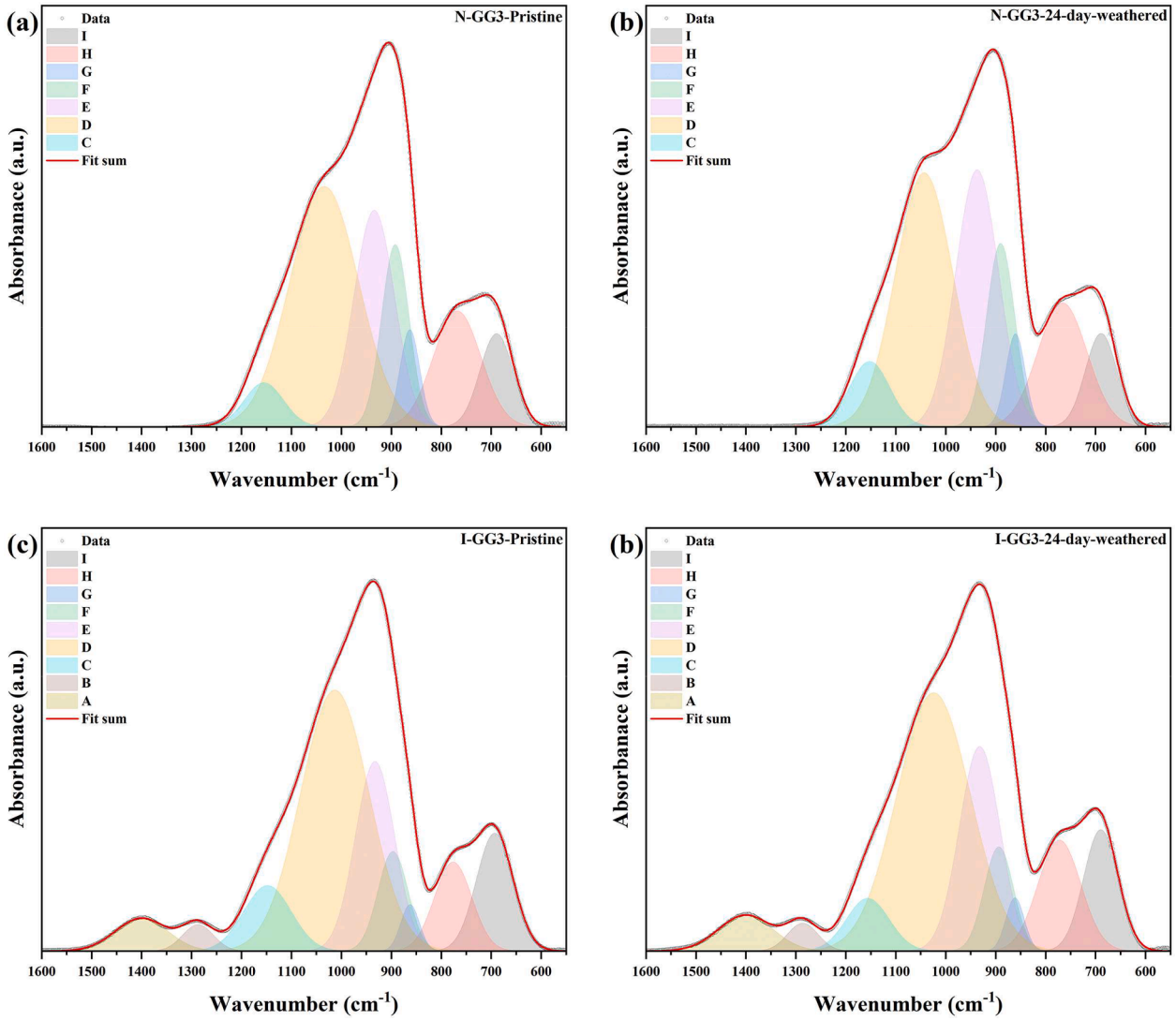

Fig. 9. FTIR normalized spectra for (a) N-GG3-Pristine, (b) N-GG3–24-day-weathered, (c) I-GG3-Pristine, and (d) I-GG3–24-day-weathered.

cohesive solid. This proves the repolymerizing silica gel evolved into a rigid, cohesive solid. Conversely, the Boson peak in I-GG3 remains stagnant (negligible -0.3 cm^{-1} shift). This stagnation implies a decoupling between chemical connectivity and physical stiffness. Despite formation of Si-O-Si bonds detected by FTIR, the I-GG3 surface layer retains a porous topology that lacks a bulk mechanical modulus.

Finally, a unique anomaly specific to strengthened glass is exhibited by the high-frequency shoulder (Band C, Fig. 9a-d, Table 3). While this band remains positionally static in native glass, a significant blue shift (+7.2 cm^{-1}) is displayed by I-GG3 upon weathering. Coupled with the negative shift observed in mixed T-O-T modes (Band m, -4.3 cm^{-1}, Fig. 10a-d, Table 3), these opposing shifts provide the molecular blueprint of the network depolymerization model.

The blue shift in Band C (Fig. 9a-d, Table 3) reflects formation of localized condensation of silica clusters (Q^4). However, this localized stiffening is mechanically negated by behavior of Band m (Fig. 10a-d, Table 3), which represents connective joints of the network (Si-O-Al/B linkages). In sharp contrast to native glass, where Band m (Fig. 10a-d, Table 3) exhibits a positive shift (+4.9 cm^{-1}), indicating that intermediate linkages participate in global gel densification, a negative shift is displayed by I-GG3. This indicates alkaline attack, where high-pH environments selectively hydrolyze and weaken intermediate bonds connecting silica islands. This phenomenon confirms formation of a phase-separated hydrogel structure in strengthened glass, preventing global densification observed in its native precursor.

3.3. Impact of weathering on optical transmittance

Changes in optical transparency reflect bulk photochemical effects, surface topography, and sub-surface compositional evolution. As illustrated in the UV–Vis spectra (Fig. 11), a progressive reduction in average transmittance is exhibited by both N-GG3 and I-GG3 over the 24-day weathering period (Fig. 11d). This optical decay is governed by three synergistic mechanisms: bulk solarization, surface scattering and volumetric evolution of compositionally altered surface layer.

A complex interaction between trace transition metal impurities (Fe and Sn) and glass processing history is involved in reduction of transmittance across the visible spectrum [34]. In pristine N-GG3, a specific transmission window (or spectral peak) between 250 and 300 nm (peak at ~280 nm) is defined by these impurities. Upon weathering, ionization of these species (solarization) is caused by high-energy photons supplied by a xenon arc source, generating stable color centers that chemically close this window [31]. However, this distinct spectral feature is already suppressed in the pristine I-GG3. Optical effects of solarization are mimicked by the ion-exchange process itself, specifically by thermal exposure at 420°C and high lattice strain, effectively shifting absorption edge and altering the local chemical environment of the impurities before weathering begins. Consequently, while the disappearance of this

Table 3
Quantitative deconvolution of vibrational spectroscopic features for N-GG3 and I-GG3 before and after 24 days of weathering.

Label	Approx. wavenumber (cm^{-1})				Assigned bond/mode	Structural significance	Ref.
FTIR							
	Pristine N-GG3	24-day weathered N-GG3	Pristine I-GG3	24-day weathered I-GG3			
A	–	–	1400.7 ±0.8	1399.9 ±0.8	B-O$^-$ Stretching / Metaborate units	Stretching vibrations involving trigonal boron (B(III)) units, such as B-O$^-$ stretching in metaborate rings. Definitive marker for $BO_4 \rightarrow BO_3$ conversion	[72, 73]
B	–	–	1287.0 ±0.6	1285.4 ±1.4	Asymmetric B-O$^-$ stretching in trigonal BO_3 (BO_2O^-) units	The lower-frequency component of the B(III) signature and related to peak A, indicating borate network reorganization in different types of metaborate configurations.	[72, 73]
C	1150.0 ±5.8	1151.2±1.6	1148.2 ±4.6	1155.4±0.8	High-frequency T-O-T stretch (Q^4 Si-O-Si)	High-frequency shoulder representing the most polymerized silica-like (Q^4) Si-O-Si linkages.	[74, 75]
D	1025.8 ±12.3	1050.6±7.2	1011.0 ±5.0	1028.0±10.0	Main T-O-T asymmetric stretch / Q^n Convolution	Main asymmetric stretching envelope of the T-O-T (T=Si, Al) network. A convolution of Si-O-Al and Si-O-Si (Q^4, Q^3) linkages.	[74, 76]
E	931.3 ±3.8	941.6±4.0	930.7 ±1.7	936.1±5.9	Si-O$^-$ stretching (Q^3/Q^2 species)	Asymmetric stretching of NBOs (Si-O$^-$) on intermediate silicate tetrahedra. This region also receives contributions from B-O$^-$ stretching in modified borate units.	[75, 76]
F	890.9 ±1.1	891.2±1.0	894.7 ±1.9	897.0±3.5	Si-O$^-$ stretching (Q^1 species)	Asymmetric stretching of NBOs on highly depolymerized silicate Q^1 units.	[75, 76]
G	862.5 ±0.8	860.4±0.1	862.0 ±0.6	862.0±0.7	Si-O$^-$ stretching (Q^0 species)	Asymmetric stretching of NBOs on orthosilicate (monomer) units. This is the most depolymerized silicate unit.	[76, 77]
H	767.5 ±1.1	764.6±3.0	772.6 ±3.2	772.0±0.6	T-O-T symmetric stretching (Si-O-Si / B-O-T)	Collective symmetric stretching and deformation modes of the T-O-T network. Represents a complex overlap, notably including stretching modes of borate units.	[72, 75, 78]
I	689.7 ±1.1	688.6±0.8	689.9 ±2.5	688.6±0.8	Antisymmetric stretching of $[AlO_4]^-$ tetrahedra.	Stretching vibrations of the Al−O bonds within the $[AlO_4]^-$ tetrahedra.	[74, 77, 79]
Raman							
j	1074±1.4	1074.7±0.9	1103.8 ±4.6	1104.5±2.3	Symmetric Si-O$^-$ (Q^3) and/or B-O stretching.	Symmetric stretching of NBOs on silicate Q^3 units AND symmetric stretching in tetrahedral $[BO_4]^-$ units. This is a composite signal reflecting moderate depolymerization and tetrahedral boron speciation.	[73, 80, 81]
k	960.8 ±1.4	961.3±1.1	1004.3 ±5.5	1002±2.6	Symmetric Si-O$^-$ (Q^2) and/or B-O$^-$ stretching	Symmetric stretching of NBOs on silicate Q^2 units AND symmetric stretching in depolymerized trigonal B units. Reflects higher localized depolymerization.	[73, 80, 82]
l	769.2 ±2.5	770.2±0.9	767.4 ±1.9	763.6±0.9	T-O-T symmetric stretching / 6-membered rings with $[BO_4]^-$	Symmetric T-O-T (T=Si, Al) stretching motion. This band is also assigned to the breathing mode of 6-membered rings containing one $[BO_4]^-$ tetrahedron.	[70, 73]
m	652.1 ±2.4	657±0.5	647.2 ±4.2	642.9±0.9	Mixed T-O-T modes	Vibrations involving mixed Al-O-Si, B-O-Si linkages and sensitive to the content of network formers (T=Si, Al, B).	[83, 84]
n	576±0.1	577.1±0.4	577±0.6	578.1±0.2	D_2 defect line (Three-membered T-O-T rings)	Symmetrical breathing mode of small, strained 3-membered mixed-cation rings (Si, Al, B), indicative of medium-range disorder.	[73, 81]
o	484.7 ±0.4	483±1.6	478.7 ±0.1	478.9±0.9	D_1 defect line (four-membered T-O-T rings)	Symmetrical breathing mode of 4-membered mixed-cation rings (Si, Al, B).	[73, 81]
p	428.1 ±2.2	429±5.6	408.3 ±0.9	409.1±3.2	T-O-T bending/rocking	Broad envelope of collective rocking and bending motions of bridging oxygen atoms in the T-O-T network (T=Si, Al, B).	[75, 83]
q	66.8±3.2	77.8±1.6	54.7±2.2	54.4±5.5	Boson peak / acoustic modes	Low-frequency band related to medium-range disorder, acoustic modes, and cation-network interactions.	[74, 81]

UV peak due to photochemical aging is manifested by N-GG3, a lower baseline in this region driven by its manufacturing history is exhibited by I-GG3.

A critical divergence in performance is observed at 380 nm wavelength (Fig. 11c), where significantly more severe transmission loss is exhibited by N-GG3 compared to I-GG3. This is driven by specific physics of the degradation models: gel densification of N-GG3 versus network depolymerization of I-GG3. To quantify these differences, the Bennett-Porteus scalar scattering theory [85] estimates the Total Scattering Loss (TS):

$$TS \approx \left(\frac{2\pi(n-1)\sigma}{\lambda}\right)^2 \quad (6)$$

where λ is the incident wavelength, n is the refractive index of the glass (≈1.5), and σ represents the Root Mean Square (RMS) roughness, denoted herein as the areal parameter S_q. A quadratic dependency is revealed by this equation, meaning that *TS* increases with the square of roughness (S_q^2).

Degradation in N-GG3 follows a gel densification model, where spontaneous repolymerization shrinks the network into a rigid silica layer. Crucially, volumetric shrinkage is caused by this densification. In the absence of a compressive stress to counteract this contraction, a tensile feedback loop at surface flaws is immediately driven by capillary forces. Formation of deep, stochastic pits ($S_q \approx 98$ nm) results with this mechanism. When applied to Eq. (6), a calculated *TS* factor of ~0.66 at 380 nm results from this high roughness.

In contrast, I-GG3 follows a network depolymerization model. Spectroscopic evidence confirms that the silicate network in I-GG3 also attempts to heal via condensation (repolymerization). However, the outcome is fundamentally different. Due to extensive depletion of near surface K^+ ions and intermediate network formers (Al, Mg), the lattice is left with significant vacancies. Consequently, while bonds shorten, effective collapse of the bulk network into a dense solid cannot occur. Hence, the surface remains as a chemically stratified, porous structure. Despite this network depolymerization, vertical crack growth is suppressed by massive compressive stress (~780 MPa). Instead of pitting, a uniform etching happens on the surface, resulting in a significantly smoother topography ($S_q \approx 74$ nm) and a much lower TS factor of 0.37.

Layer depth also plays a role. Chemical alteration is restricted to a thinner layer by kinetic constraints in I-GG3 compared to deep depletion

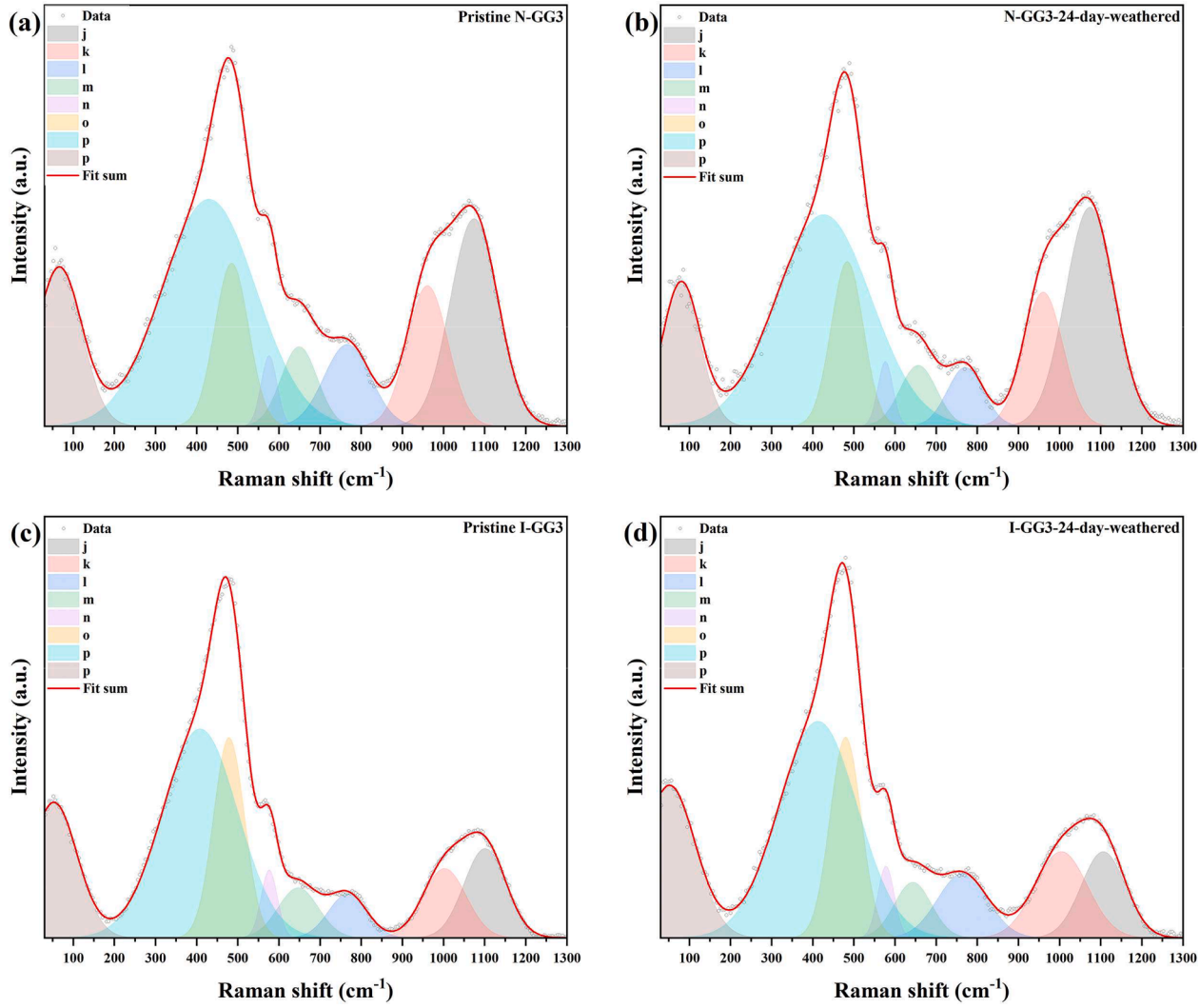

Fig. 10. Micro-Raman normalized intensity spectra for (a) N-GG3-Pristine, (b) N-GG3–24-day-weathered, (c) I-GG3-Pristine, and (d) I-GG3–24-day-weathered.

observed in N-GG3. Thus, transparency is preserved by I-GG3 not only by maintaining a smoother surface via compressive shielding but also by minimizing the total volume of the optically degraded phase.

3.4. Evolution of mechanical properties

Macroscopic mechanical measurements validate the observed structural changes. The analysis of surface stress, hardness, scratch resistance, and K_{IFT} reveal a critical paradox: while the results in Fig. 12 demonstrate that the strengthening profile remains intact throughout the weathering process of I-GG3 samples, deteriorations in other mechanical properties are observed.

This apparent stability reflects a measurement limitation rather than an absence of surface degradation. Since the FSM-6000LE stressmeter operates via the optical waveguide effect, integration of stress response over the full depth of that layer, which in many cases spans 5–50 μm, is required by this measurement [24,86]. However, weathering-induced degradation, specifically ion leaching and hydrogel formation, is confined to immediate surface layer (<1 μm). The instrument detects the sub-surface stress reservoir, masking the failure of the outer hydrated layer. Stress profile stability is therefore an artifact of penetration depth; depth-sensing indentation (Vickers) is required to reveal near-surface softening. Stress meters fail to detect these shallow changes, reading the intact bulk stress rather than the compromised surface.

While the deep stress profile appears stable, Vickers hardness tests reveal near-surface mechanical vulnerability (Fig. 13). In pristine state, efficacy of the ion-exchange process is evident, with I-GG3 exhibiting significantly higher hardness (~6.15 GPa) compared to N-GG3 (~5.65 GPa). However, a significant divergence in degradation trajectories is observed. Native glass displays a stable response with minor hardness decrease, implying a compensatory mechanism linked to gel densification. While surface softening is typically caused by hydration, the Al-catalyzed repolymerization of the surface creates a dense, ceramic-like layer. This chemically stiffened layer resists plastic deformation effectively, resulting in a relatively flat hardness profile compared to the I-GG3 hydrogel.

In contrast, a two-stage failure mode is revealed by I-GG3 hardness profile. After a period of relative stability, a sharp drop in hardness between Day 12 and Day 24 is observed, falling to ~5.90 GPa. This accelerated softening corresponds to thickening of a gel layer identified in spectroscopic analysis. Boson peak stagnation (Fig. 10, Table 3) and mixed-cation linkage softening imply a porous, hydrated surface layer lacking the stiffening seen in native glass. By Day 24, this hydrogel alters contact mechanics; the indenter penetrates the compromised shell, registering lower hardness despite the intact substrate. It is important to distinguish between surface contact stiffness and bulk fracture tolerance. The formation of the porous hydrogel layer reduces the effective elastic modulus of the surface, resulting in a decrease in Vickers microhardness (surface softening). However, macroscopic damage tolerance is governed by the deep residual compressive stress profile,

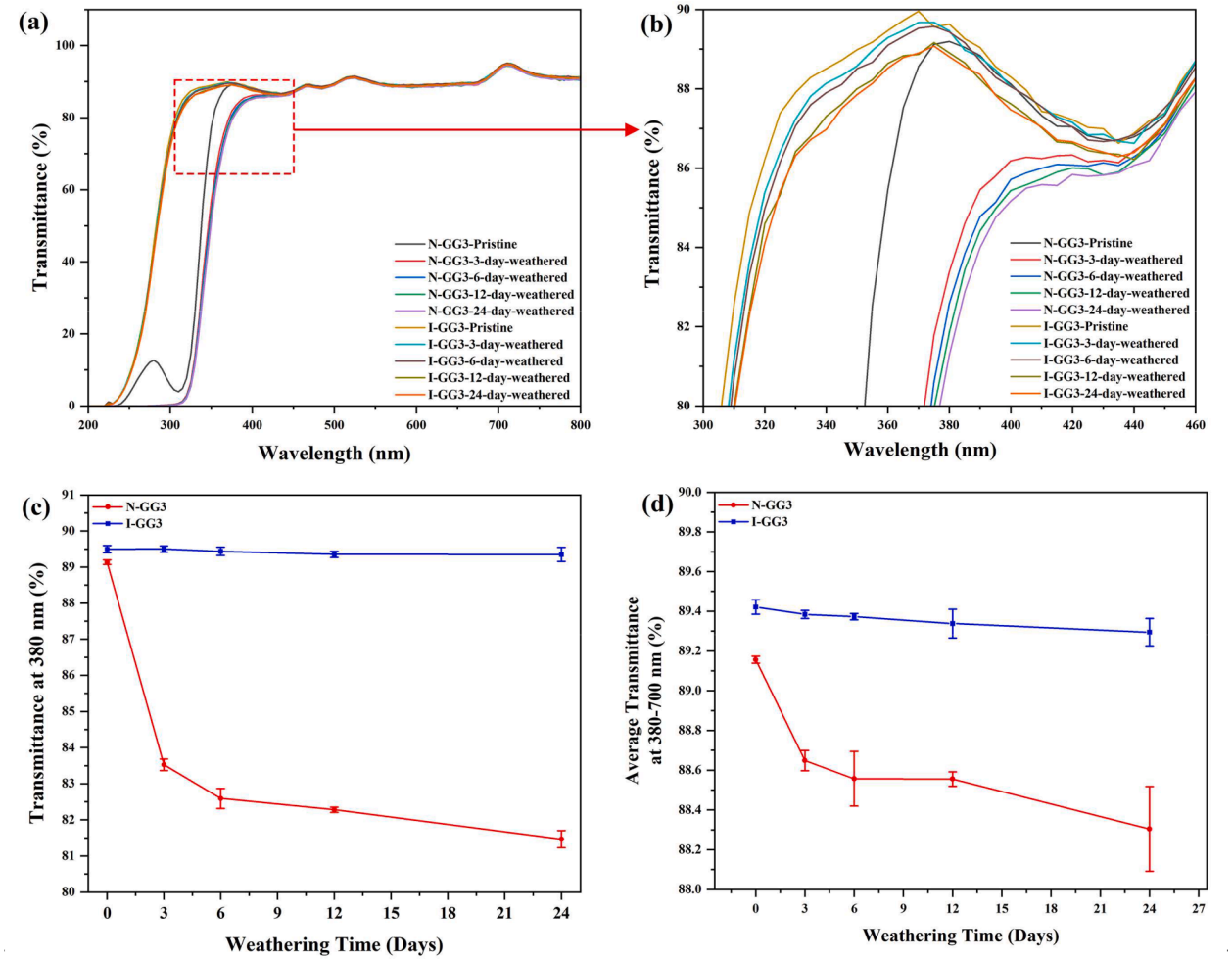

Fig. 11. (a, b) UV–Vis transmittance spectra for N-GG3 and I-GG3 samples at different weathering durations, (c) transmittance at 380 nm and (d) average transmittance at 380–700 nm as a function of weathering time.

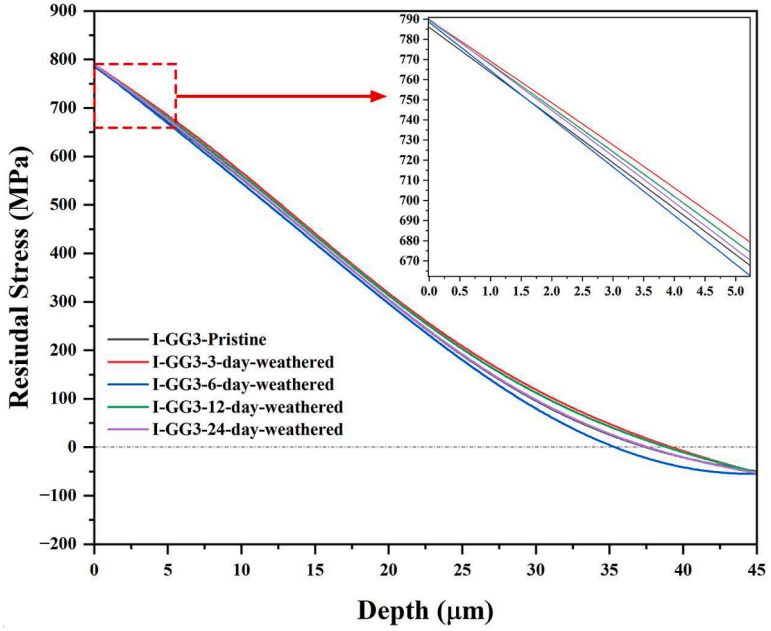

Fig. 12. Evolution of surface compressive stress as a function of depth for I-GG3 samples subjected to different weathering durations.

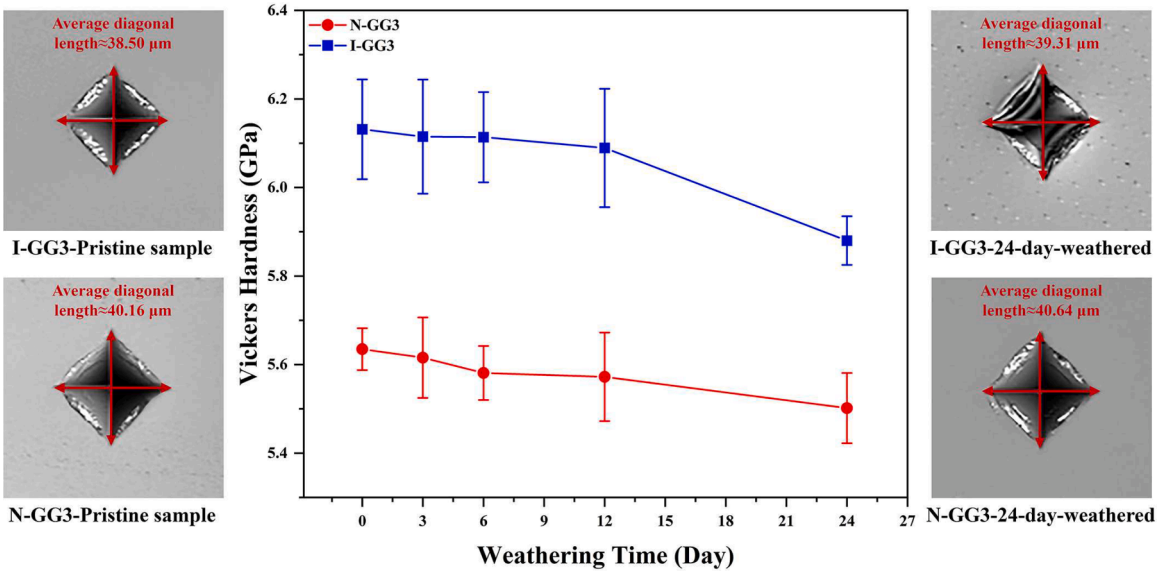

Fig. 13. Vickers hardness as a function of weathering time for N-GG3 and I-GG3 samples.

which effectively arrests any surface flaws initiated within the soft gel, preventing vertical propagation and forcing the material to fail via shallow lateral dissolution (etching) rather than catastrophic fracture.

Surface modification also impacts dynamic failure modes (scratch testing, Figs. 14, 15). The First Critical Load (L_{c1}, Fig. 14), which identifies the threshold for brittle chipping or cracking, serves as a metric for surface flaw sensitivity. Consistent with its superior hardness, the pristine I-GG3 exhibits a higher L_{c1} (~350 mN) compared to the native glass (~220 mN), illustrating the direct benefit of the compressive stress layer in inhibiting crack initiation. This illustrates the benefit of the compressive stress layer in inhibiting crack initiation. Under weathering, a significant reduction in L_{c1} is shown by N-GG3, dropping to ~180 mN. Increased roughness and pitting density lower the fracture threshold, as deep pits act as stress concentrators. Conversely, a remarkably stable L_{c1} is maintained by I-GG3 throughout the weathering process. This resilience is attributed to the preserved compressive stress and smoother topology, preventing stress-concentrating defects despite surface softening.

Failure mechanisms are further elucidated by representative scratch tracks (Fig. 15). All samples show smooth plastic deformation grooves at low loads (Fig. 15a-c). However, a jagged, irregular scratch path with early onset of lateral micro cracks and chipping is displayed by N-GG3 (Fig. 15a, b), indicative of a brittle, flaw-sensitive surface. In contrast, the scratch track on I-GG3 (Fig. 15c, d) remains comparatively smooth and uniform before the onset of chipping, demonstrating the effective compressive stress shielding against crack propagation.

Finally, the apparent K_{IFT} of the native glass (N-GG3) trends downward (Fig. 16b), derived from increasing crack lengths (Fig. 16a). It should be noted that the initial K_{IFT} value (~1.07 MPa $m^{1/2}$) is elevated relative to the intrinsic toughness of native GG3 (~0.66 MPa $m^{1/2}$). This overestimation is a known artifact of using a fixed-coefficient indentation method on highly densifying materials. During indentation, glasses with higher silica content deform primarily through localized densification (volumetric compaction) rather than volume-displacing shear.

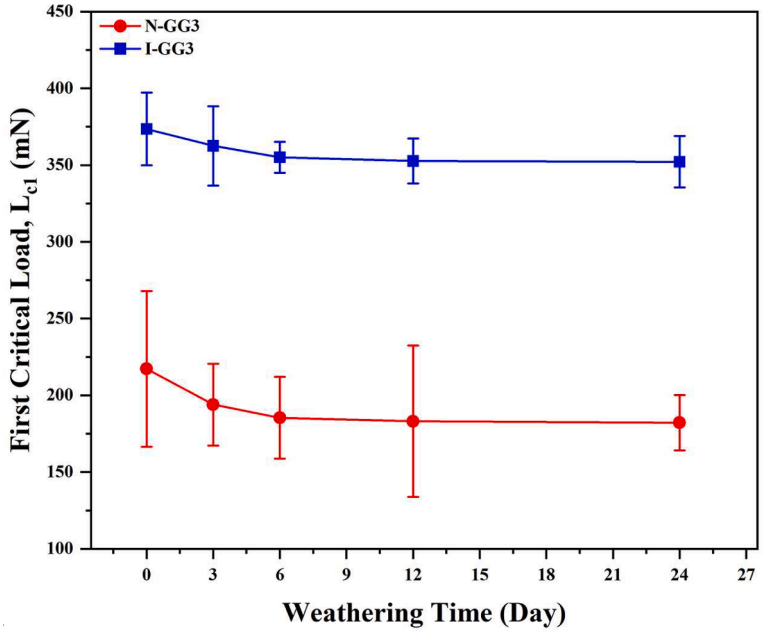

Fig. 14. First critical load as a function of weathering time for N-GG3 and I-GG3 samples.

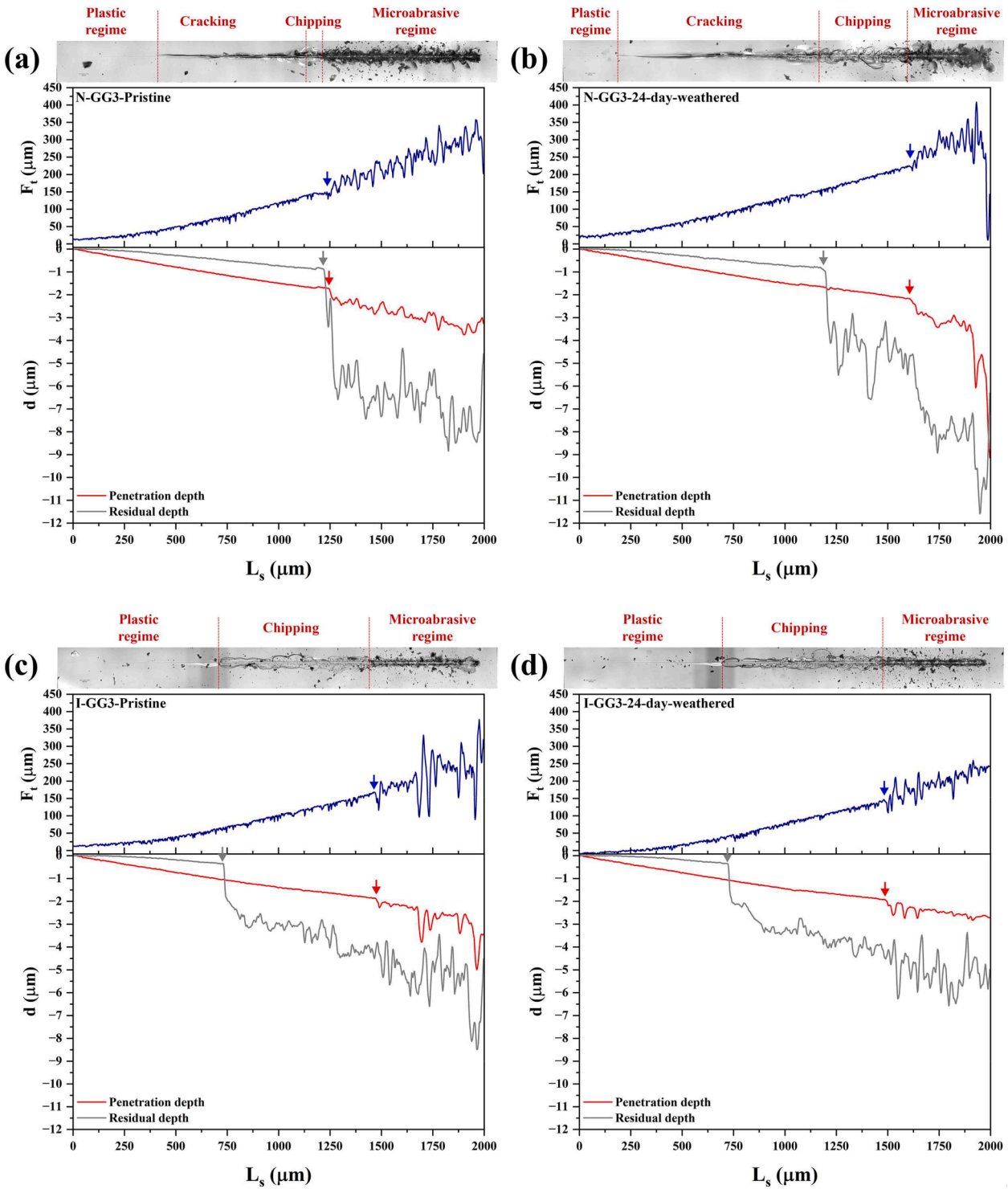

Fig. 15. Representative ramp-load scratch test results showing tangential force (F_t), penetration depth, and residual depth versus scratch length (L_s) for (a) N-GG3-Prisitne, (b) N-GG3–24-day-weathered, (c) I-GG3-Prisitne, and (d) I-GG3–24-day-weathered.

This shift toward densification substantially diminishes the residual tensile stress field generated in the region surrounding the indent. Because this residual stress is what normally drives median and radial crack propagation, the reduced stress field results in stunted crack growth (shorter crack lengths). When these artificially short crack lengths are used in the standard equation, it leads directly to a formulaic overestimation of the material's actual toughness [87]. However, as a comparative metric for benchmarking degradation, the K_{IFT} effectively captures the evolution of near-surface stresses. Because the measured value represents a superposition of these stress fields, the reduction in apparent damage tolerance is a direct consequence of the morphological degradation identified in Section 3.1. Polymerization shrinkage induces localized tensile stresses which superimpose on the indentation stress field. When combined with a high density of surface pits acting as stress concentrators (Griffith flaws), the energy barrier for crack propagation is lowered by this tensile field. Consequently, N-GG3 becomes increasingly brittle and susceptible to fracture, contrasting with I-GG3 where formation and growth of such radial cracks continues to be effectively

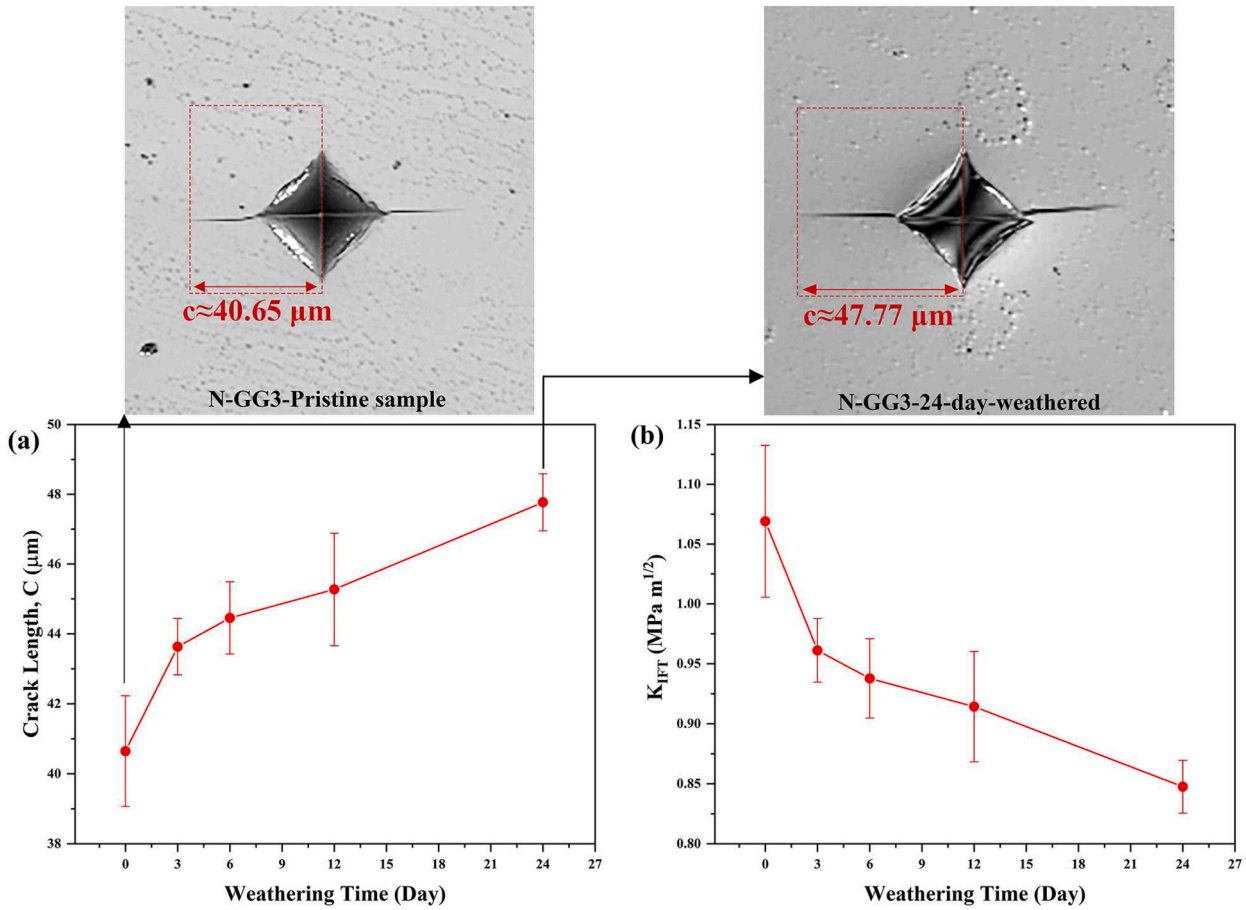

Fig. 16. (a) Crack length measurements and (b) K_{IFT} as a function of weathering time for N-GG3 samples.

suppressed by the engineered compressive stress profile.

3.5. Comparative degradation behavior and mechanisms

Multi-modal characterization reveals that ion exchange alters the thermodynamics and kinetics of degradation, acting as more than just a mechanical shield. Following common initial alkali depletion, the mechanisms diverge into distinct gel densification and network depolymerization models.

Degradation of N-GG3 is governed by kinetic moderation and physical drying mechanisms analogous to sol-gel processing. A critical prerequisite for this model is the chemical stability of the aluminosilicate network. As indicated by TOF-SIMS (Fig. 6), while sodium acts as a mobile charge compensator for $[AlO_4]^-$ units, its leaching occurs in a near-neutral pH environment maintained by the cyclic spray washout. Consequently, the intermediate network formers (Al, Mg) are retained, likely due to the near-neutral pH preventing the formation of soluble aluminate species. Aluminum retention is pivotal; it acts as a structural network and lowers the activation energy for siloxane bond reformation, catalyzing network self-healing during drying [61].

During the dry periods of the accelerated weathering protocol (63°C, 30 % relative humidity), this stabilized layer undergoes structural consolidation via the condensation of vicinal silanol groups:

$$2(\equiv Si-OH) \leftrightarrow (\equiv Si-O-Si \equiv) + H_2O(g) \quad (7)$$

Although precise thermodynamic data for transient surface species is scarce, the drivers of this mechanism are clear. The low relative humidity (30 %) constantly removes the water vapor product, shifting the chemical equilibrium toward bond formation. This thermodynamic drive is then kinetically accelerated by mechanical forces.

Evaporation of pore water from the nanometric voids of the leached layer generates immense capillary pressure (P_c). Because the leached layer possesses low permeability, this capillary action exerts a strong compressive stress on the pore walls, physically forcing neighboring silanol groups into reaction distance (forced condensation) [88,89]. Quantification of this driver was realized by applying the Young-Laplace equation to the nanometric pores of the hydrated gel [89]:

$$P_c = \frac{2\gamma cos\theta}{r} \quad (8)$$

where γ represents the surface tension of the pore liquid, θ is the contact angle, and r is the pore radius. Using the surface tension of water at the drying temperature of 63°C ($\gamma \approx 0.066$ N/m [90]), assuming perfect wetting ($\cos\theta \approx 1$), and a typical pore radius (r) of 2 nm, a capillary pressure (P_c) of approximately 66 MPa is calculated acting on the gel skeleton.

However, a critical mechanical paradox emerges from this aggressive densification. While syneresis (gel contraction) drives volumetric shrinkage, the surface layer is chemically bonded to the rigid, non-shrinking bulk glass substrate. This substrate constraint prevents in-plane contraction. Consequently, the compressive densification of the pore structure translates globally into a high biaxial tensile stress field across the surface leached layer [89]. This induced tension lowers the activation energy for crack propagation at micro-flaws, driving the stochastic pitting and brittleness observed in N-GG3. This interpretation is validated by the blue shift in FTIR spectra (Fig. 9a, b), which signifies bond stiffening, and the substantial positive shift of the Raman Boson peak (Band q), confirming the evolution of the gel into a rigid, densified network.

In contrast, I-GG3 degradation is driven by a mechanochemical

Instability. The ion-exchange layer acts as a high-energy reservoir where stuffed K^+ ions create significant lattice strain. Internal pressure necessitates topological reconfiguration. The spectroscopic shift from tetrahedral [BO_4] to trigonal [BO_3] coordination accommodates the ion-exchange induced dilation, manifested by the emergence of bands A (~1400 cm^{-1}) and B (~1287 cm^{-1}) in the I-GG3 FTIR spectrum (Fig. 9c). The substitution of larger K^+ ions generates steric crowding. To accommodate the excess volume, the rigid [BO_4] network relaxes into the planar [BO_3] configuration, effectively ring-opening the network to generate the necessary free volume for housing the invading cation. This structural relaxation creates a chemical vulnerability, as planar [BO_3] units have a lower activation energy for hydrolysis than [BO_4] tetrahedra, facilitating rapid potassium leaching upon moisture exposure. Consequently, upon weathering, a burst release of alkali spikes the local pH (>9). Under these alkaline conditions, dissolution of the stabilizing aluminosilicate network occurs, as evidenced by deep depletion of Al and Mg. Modification of the gel densification mechanism is significantly caused by loss of Al. As observed in FTIR analysis (Section 3.2), an attempt to repolymerize is still made by the silicate network (evidenced by minor blue shift, see Fig. 9c, d). However, without intermediate network formers to bridge gaps and given a high density of lattice vacancies, translation of this chemical connectivity into topological densification cannot occur.

Instead of densifying into a rigid layer, the surface evolves into a chemically loosened hydrogel (Fig. 17b, Stage 3). Nevertheless, this porous layer is still subject to physical forces of drying. To determine if capillary effects drive fracture, the net stress (σ_{net}) was calculated by superimposing residual capillary tension (P_c) onto the engineered stress profile:

$$\sigma_{net} = \sigma_{CS} + P_c \tag{9}$$

With $\sigma_{CS} \approx$ -780 MPa and assuming similar capillary suction of $P_c \approx$ 66 MPa is generated at same drying conditions, the resulting σ_{net} remains overwhelmingly compressive at approximately -714 MPa. Thus, the driving force for fracture is effectively neutralized even in presence of localized capillary tension. Vertical crack growth is suppressed, and degradation is forced into the observed uniform etching mode (Fig. 18b).

4. Conclusion and outlook

This study analyzes the time-dependent degradation mechanisms of ion-exchanged boroaluminosilicate glass (I-GG3) versus its native precursor (N-GG3). By correlating nanoscale chemical kinetics with macroscale mechanical responses, two divergent failure pathways were identified, governed by the thermodynamic stability of the glass network:

Divergent mechanochemical pathways: The degradation outcome is dictated by the stability of the intermediate aluminosilicate network. In N-GG3, the retention of Al and Mg facilitates a gel densification mechanism, where hydrolytic repolymerization and capillary-driven

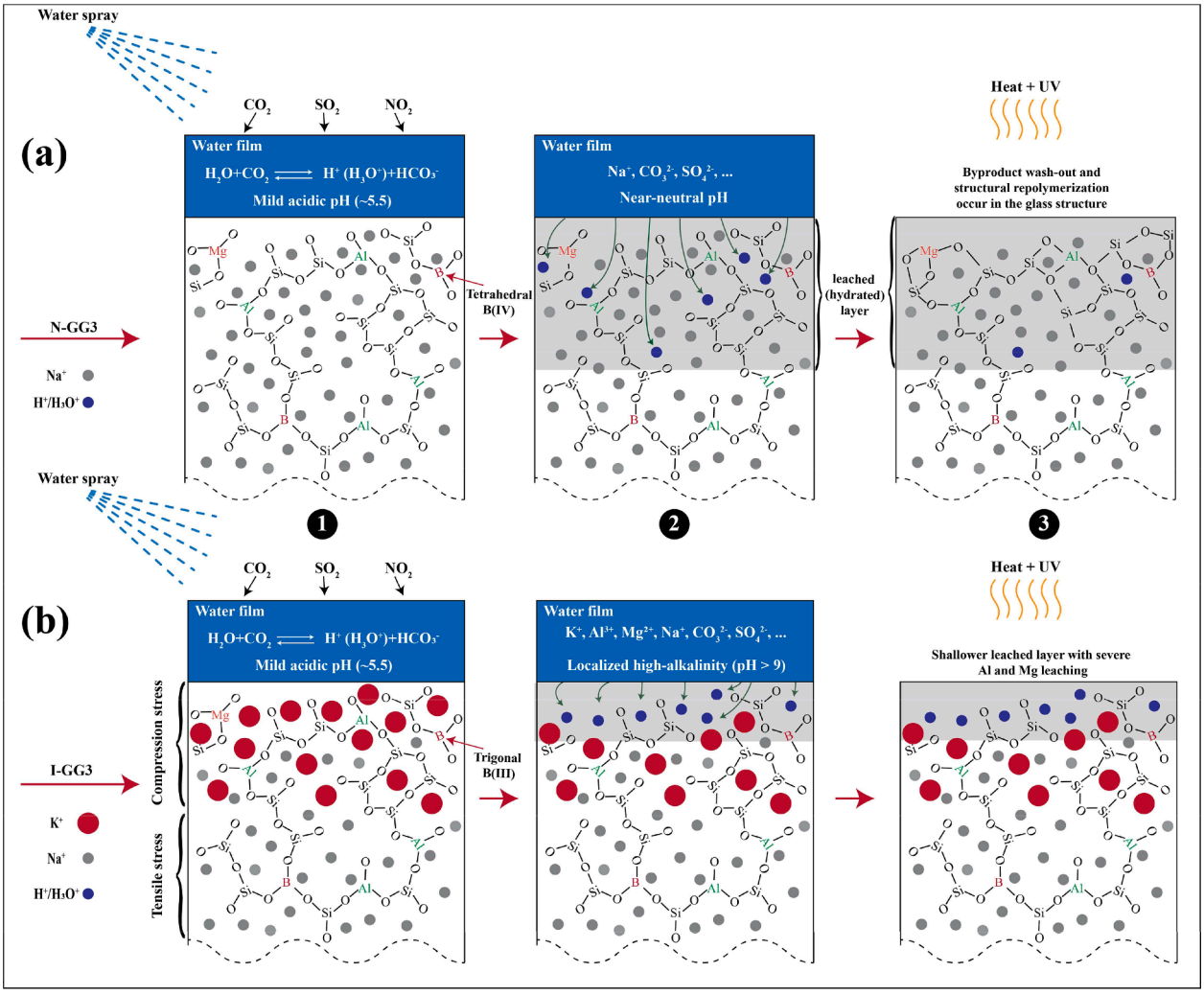

Fig. 17. Schematic diagram depicting the divergent degradation pathways for (a) N-GG3 (gel densification model) and (b) I-GG3 (network depolymerization model), wherein the distinct structural evolution of the glass surface under accelerated weathering is elucidated.

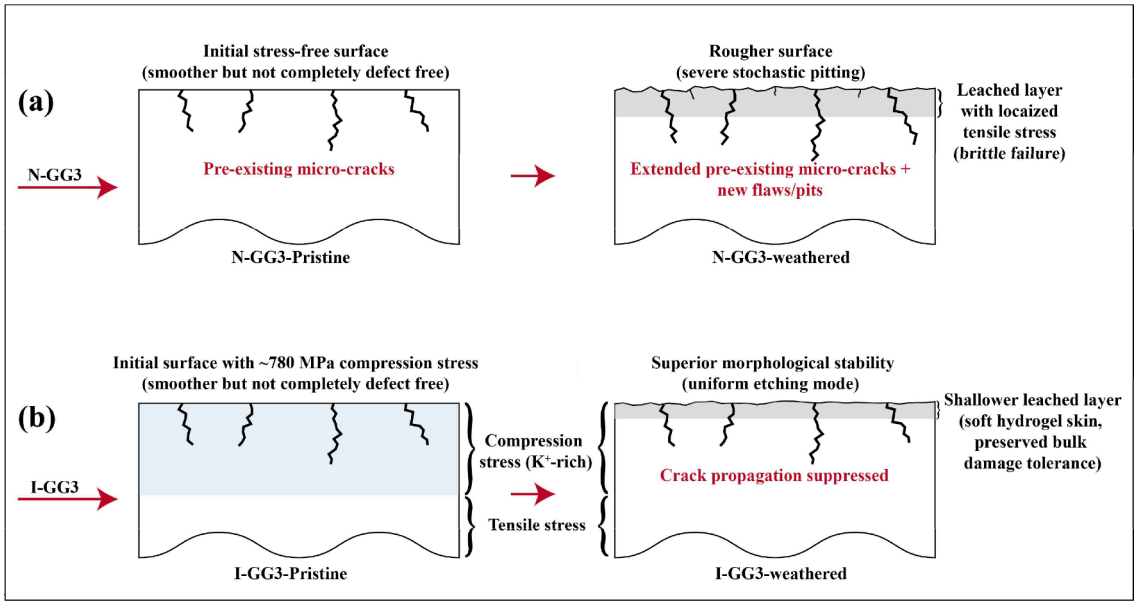

Fig. 18. Comparative visualization of resultant surface topographies exhibiting (a) stochastic pitting and crack growth in N-GG3 driven by capillary forces and (b) uniform etching in I-GG3 resulting from the mechanical suppression of vertical crack growth.

syneresis create a densified, silica-rich leached layer. Conversely, the rapid alkaline release in I-GG3 triggers a network depolymerization mechanism. High pH dissolves the Al/Mg network, preventing densification and yielding a porous, potassium-depleted hydrogel.

Boron coordination change: Spectroscopic analysis reveals that the ion-exchange process predisposes the glass to network depolymerization. The conversion of rigid [BO_4] units to planar [BO_3] units to accommodate K^+ ions increases susceptibility to hydrolysis and water diffusion.

Topological control via compressive stress: Despite network depolymerization, the residual compressive stress (~780 MPa) in I-GG3 suppresses vertical crack propagation and stochastic pitting. This forces degradation into uniform etching, minimizing Rayleigh scattering and preserving transmittance despite decreased hardness.

Metrology implications: Standard surface stress meters (e.g., FSM-6000) produce artifacts when measuring degraded surfaces. These optical waveguide devices integrate stress over the full depth of the ion-exchanged layer (>40 μm) and consequently fail to detect the formation of the mechanically compromised hydrogel leached layer (<1 μm). This requires depth-sensing indentation or near-surface spectroscopy for accurate lifetime prediction.

These findings suggest that chemical strengthening fundamentally modifies the glass-water reaction pathway, rather than acting solely as a mechanical shield.

Declaration of generative AI and AI-assisted technologies in the writing process

During the preparation of this work the authors used Gemini Pro 2.5 model in order to assist with grammar, spelling, punctuation, and overall sentence structure, enhancing the clarity and flow of the text. After using this tool/service, the authors reviewed and edited the content as needed and take full responsibility for the content of the published article.

Data statement

Data will be made available on request.

CRediT authorship contribution statement

Seyed Ali Delbari: Writing – review & editing, Writing – original draft, Visualization, Validation, Software, Methodology, Investigation, Formal analysis, Data curation, Conceptualization. **Lucas A. Hof:** Writing – review & editing, Validation, Supervision, Resources, Project administration, Methodology, Funding acquisition, Conceptualization.

Declaration of competing interest

The authors declare that they have no known competing financial interests or personal relationships that could have appeared to influence the work reported in this paper.

Acknowledgements

This research was supported by the Natural Sciences and Engineering Research Council of Canada (NSERC) under the Discovery Grant (RGPIN-2019-05973).

References

[1] R. Balzer, H. Behrens, T. Waurischk, S. Reinsch, R. Müller, P. Kiefer, J. Deubener, M. Fechtelkord, Water in Alkali aluminosilicate glasses, Front. Mater. 7 (2020), https://doi.org/10.3389/fmats.2020.00085.
[2] Y. Xiang, J. Du, M.M. Smedskjaer, J.C. Mauro, Structure and properties of sodium aluminosilicate glasses from molecular dynamics simulations, J. Chem. Phys. 139 (2013), https://doi.org/10.1063/1.4816378.
[3] C.L. Losq, A.P. Valentine, B.O. Mysen, D.R. Neuville, Structure and properties of alkali aluminosilicate glasses and melts: insights from deep learning, Geochim. Cosmochim. Acta 314 (2021) 27–54, https://doi.org/10.1016/j.gca.2021.08.023.
[4] D.M. Zirl, S.H. Garofalini, Structure of sodium aluminosilicate glasses, J. Am. Ceram. Soc. 73 (1990) 2848–2856, https://doi.org/10.1111/j.1151-2916.1990.tb06685.x.
[5] S.A. Delbari, J.-P. Leclair, G. Villeneuve, L.A. Hof, High-quality freeform machining of chemically strengthened glass using spark assisted chemical engraving, Results. Eng. 29 (2026) 109591, https://doi.org/10.1016/j.rineng.2026.109591.
[6] J.C. Tait, D.L. Mandolesi, The Chemical Durability of Alkali Aluminosilicate Glasses, Atomic Energy of Canada Ltd. No. AECL–7803, 1983.
[7] S. Yoshida, A. Hidaka, J. Matsuoka, Crack initiation behavior of sodium aluminosilicate glasses, J. Non. Cryst. Solids. 344 (2004) 37–43, https://doi.org/10.1016/j.jnoncrysol.2004.07.019.
[8] P.I.K. Onorato, M.N. Alexander, C.W. Struck, G.W. Tasker, D.R. Uhlmann, Bridging and nonbridging oxygen atoms in alkali aluminosilicate glasses, J. Am. Ceram. Soc. 68 (1985), https://doi.org/10.1111/j.1151-2916.1985.tb15223.x.

[9] S. Huang, W. Wang, H. Jiang, H. Zhao, Y. Ma, Network structure and properties of lithium aluminosilicate glass, Materials 15 (2022) 4555, https://doi.org/10.3390/ma15134555.
[10] E.M.A. Hussein, S.E. Shaban, A.M. Madbouly, Chemical durability and shielding study of borosilicate glass systems from solid municipal waste ash for radiation shielding applications, Opt. Quantum. Electron. 56 (2024) 543, https://doi.org/10.1007/s11082-023-06180-y.
[11] M. Hubert, A.J. Faber, On the structural role of boron in borosilicate glasses, physics and chemistry of glasses, Eur. J. Glass Sci. Technol. B 55 (2014) 136–158.
[12] J. Marcial, J. Kabel, M. Saleh, Y. Shaharyar, A. Goel, J. McCloy, Effect of B on crystallization of Li and Na aluminosilicates, in: WM2016 Conference, Phoenix, Arizona, 2016.
[13] J. Ramkumar, V. Sudarsan, S. Chandramouleeswaran, V.K. Shrikhande, G. P. Kothiyal, P.V. Ravindran, S.K. Kulshreshtha, T. Mukherjee, Structural studies on boroaluminosilicate glasses, J. Non. Cryst. Solids. 354 (2008) 1591–1597, https://doi.org/10.1016/j.jnoncrysol.2007.10.005.
[14] J.G. Couillard, Boro-aluminosilicate glass for architectural applications, in: Glass Performance Days 2025 (GPD 2025), Glass Performance Days, Tampere, Finland, 2025.
[15] X. Chen, Y. Tian, W. Hu, P. Lu, B. Tan, F. Chen, Y. Zhang, A multi-step chemical ion-exchange process for alkali/alkaline-earth aluminosilicate glasses, Ceram. Int. 45 (2019) 24878–24883, https://doi.org/10.1016/j.ceramint.2019.09.050.
[16] R. Gy, Ion exchange for glass strengthening, Mater. Sci. Eng.: B 149 (2008) 159–165, https://doi.org/10.1016/j.mseb.2007.11.029.
[17] G. Macrelli, Chemically strengthened glass by ion exchange: strength evaluation, Int. J. Appl. Glass. Sci. 9 (2018) 156–166, https://doi.org/10.1111/ijag.12291.
[18] S.A. Delbari, L.A. Hof, Glass waste Circular economy - advancing to high-value Glass sheets recovery using industry 4.0 and 5.0 technologies, J. Clean. Prod. (2024) 142629, https://doi.org/10.1016/j.jclepro.2024.142629.
[19] R.F. Bartholomew, H.M. Garfinkel, Chemical strengthening of glass, in: 1980: pp. 217–270. https://doi.org/10.1016/B978-0-12-706705-6.50011-4.
[20] T.M. Gross, Chemical strengthening of glass, in: 2019: pp. 273–296. https://doi.org/10.1007/978-3-319-93728-1_8.
[21] R.D. Shannon, Revised effective ionic radii and systematic studies of interatomic distances in halides and chalcogenides, Acta Crystallogr. A 32 (1976) 751–767, https://doi.org/10.1107/S0567739476001551.
[22] A. Tandia, K.D. Vargheese, J.C. Mauro, Elasticity of ion stuffing in chemically strengthened glass, J. Non. Cryst. Solids. 358 (2012) 1569–1574, https://doi.org/10.1016/j.jnoncrysol.2012.04.021.
[23] A.K. Varshneya, Chemical strengthening of glass products, Trans. Indian Ceram. Soc. 60 (2001) 1–6, https://doi.org/10.1080/0371750X.2001.10799951.
[24] J. Mao, J. Yuan, Z. Guo, P. Tian, J. Zhang, Q. Zhang, Enhancing bending performance of ultrathin flexible glass through chemical strengthening, Int. J. Appl. Glass. Sci. 15 (2024) 267–275, https://doi.org/10.1111/ijag.16659.
[25] H. Morozumi, H. Nakano, S. Yoshida, J. Matsuoka, Crack initiation tendency of chemically strengthened glasses, Int. J. Appl. Glass. Sci. 6 (2015) 64–71, https://doi.org/10.1111/ijag.12089.
[26] S. Fujita, T. Ohji, T. Yahagi, M. Iijima, J. Tatami, Micro-scale mechanical properties of surface layer in ion-exchanged glass, J. Am. Ceram. Soc. 107 (2024) 3666–3672, https://doi.org/10.1111/jace.19755.
[27] S. Karlsson, Modification of float glass surfaces by ion exchange. Doctoral Thesis, Linnaeus University, 2012.
[28] V. Tyagi, A.K. Varshneya, Measurement of progressive stress buildup during ion exchange in alkali aluminosilicate glass, J. Non. Cryst. Solids. 238 (1998) 186–192, https://doi.org/10.1016/S0022-3093(98)00691-7.
[29] Y.A. Gösterişlioğlu, A.E. Ersundu, M. Çelikbilek Ersundu, İ. Sökmen, Investigation the effect of weathering on chemically strengthened flat glasses, J. Non. Cryst. Solids. 544 (2020) 120192, https://doi.org/10.1016/j.jnoncrysol.2020.120192.
[30] I.G. Lukachevskaia, A. Kychkin, A.K. Kychkin, E.D. Vasileva, A.E. Markov, Effect of 2000-hour ultraviolet irradiation on surface degradation of glass and basalt Fiber-reinforced laminates, Polymers 17 (2025) 1980, https://doi.org/10.3390/polym17141980.
[31] S.D. Jackson, J. Ballato, Defect centers in the silicate glasses: basics, implications, and mitigation strategies for the generation of visible light, Laser. Photon. Rev. (2025), https://doi.org/10.1002/lpor.202500872.
[32] D.K. Belashchenko, O.I. Ostrovski, Molecular dynamics simulation of oxides with ionic–covalent bonds, Thermochim. Acta 372 (2001) 143–152, https://doi.org/10.1016/S0040-6031(01)00452-X.
[33] P.R. Jubu, O.S. Obaseki, A. Nathan-Abutu, F.K. Yam, Y. Yusof, M.B. Ochang, Dispensability of the conventional Tauc's plot for accurate bandgap determination from UV–vis optical diffuse reflectance data, Results Opt. 9 (2022) 100273, https://doi.org/10.1016/j.rio.2022.100273.
[34] D. Ehrt, UV-absorption and radiation effects in different glasses doped with iron and tin in the ppm range, C. R. Chim. 5 (2002) 679–692, https://doi.org/10.1016/S1631-0748(02)01432-7.
[35] J.F. WHITE, W.B. SILVERMAN, Some studies on the solarization of glass, J. Am. Ceram. Soc. 33 (1950) 252–257, https://doi.org/10.1111/j.1151-2916.1950.tb14175.x.
[36] A.K. Varshneya, Chemical strengthening of glass: lessons learned and yet to Be learned, Int. J. Appl. Glass. Sci. 1 (2010) 131–142, https://doi.org/10.1111/j.2041-1294.2010.00010.x.
[37] M. Ciccotti, Stress-corrosion mechanisms in silicate glasses, J. Phys. D. Appl. Phys. 42 (2009) 214006, https://doi.org/10.1088/0022-3727/42/21/214006.
[38] A. TOURNIE, P. RICCIARDI, P. COLOMBAN, Glass corrosion mechanisms: a multiscale analysis, Solid. State Ion. 179 (2008) 2142–2154, https://doi.org/10.1016/j.ssi.2008.07.019.
[39] X. Ma, J. Liu, J. Zhang, Y. Su, K. Yi, Y. Zhang, L. Ding, Q. Zheng, Impact of chemical corrosion on mechanical properties of boroaluminosilicate pharmaceutical glasses, Materials 17 (2024) 3120, https://doi.org/10.3390/ma17133120.
[40] S. Reiß, S. Krischok, E. Rädlein, Comparative study of weather induced corrosion mechanisms of toughened and normal float glasses, Glass Technology, Eur. J. Glass Sci. Technol. A 60 (2019) 33–44, https://doi.org/10.13036/17533546.60.2.020.
[41] A.J.H.B.Z.R.R.V. Ellison, Ion exchangeable glass with advantaged stress profile, US 2014/0227524 A1, 2014.
[42] Corning Incorporated, Gorilla Glass 3 Product Sheet, New York, USA, 2020. https://www.corning.com/microsites/csm/gorillaglass/PI_Sheets/2020/Gorilla_Glass_3_ProdSheet.pdf (accessed March 23, 2025).
[43] H. Liu, M.M. Smedskjaer, H. Tao, L.R. Jensen, X. Zhao, Y. Yue, A medium range order structural connection to the configurational heat capacity of borate–silicate mixed glasses, Phys. Chem. Chem. Phys. 18 (2016) 10887–10895, https://doi.org/10.1039/C6CP00749J.
[44] H. Liu, Structure, phase transitions, and dynamics in four special oxide glass systems. Doctoral Thesis, Aalborg Universitet, 2018.
[45] G. El Damrawi, A.M. Abdelghany, H. Salaheldin, Effect of aluminum oxide on the structure and conduction behaviors of silver borate glasses, Bull. Chem. Soc. Ethiop. 36 (2022) 597–606, https://doi.org/10.4314/bcse.v36i3.9.
[46] S. Kohara, J. Akola, H. Morita, K. Suzuya, J.K.R. Weber, M.C. Wilding, C. J. Benmore, Relationship between topological order and glass forming ability in densely packed enstatite and forsterite composition glasses, Proc. Natl. Acad. Sci. 108 (2011) 14780–14785, https://doi.org/10.1073/pnas.1104692108.
[47] M. Hujova, Influence of fining agents on glass melting: a review, part 1, Ceram. - Silik (2017) 119–126, https://doi.org/10.13168/cs.2017.0006.
[48] J. Zhao, Y. Wang, J. Kang, Y. Qu, G.A. Khater, S. Li, Q. Shi, Y. Yue, Effect of SnO2 on the structure and chemical durability of the glass prepared by red mud, J. Non. Cryst. Solids. 509 (2019) 54–59, https://doi.org/10.1016/j.jnoncrysol.2019.01.029.
[49] V. Vercamer, G. Lelong, H. Hijiya, Y. Kondo, L. Galoisy, G. Calas, Diluted Fe3+ in silicate glasses: structural effects of Fe-redox state and matrix composition. An optical absorption and X-band/Q-band EPR study, J. Non. Cryst. Solids. 428 (2015) 138–145, https://doi.org/10.1016/j.jnoncrysol.2015.08.010.
[50] V. Vercamer, Spectroscopic and structural properties of iron in silicate glasses. Doctoral Thesis, Université Pierre et Marie Curie (UPMC), 2016.
[51] G. Calas, L. Cormier, L. Galoisy, P. Jollivet, Structure–property relationships in multicomponent oxide glasses, C. R. Chim. 5 (2002) 831–843, https://doi.org/10.1016/S1631-0748(02)01459-5.
[52] F. Sizov, Z. Tsybrii, Optical transmittance of CdTe/HgCdTe/CdZnTe structures, Phys. Chem. Solid State 26 (2025) 344–349, https://doi.org/10.15330/pcss.26.2.344-349.
[53] K. AKATSUKA, S. OGAMI, S. Ohara, S. ORIHARA, Development of measurement method for stress distribution in 2-step ion-exchanged glass, J. Ceram. Soc. Jpn. 124 (2016) S7–S11, https://doi.org/10.2109/jcersj2.16105.
[54] ASTM International, ASTM C1327-15(2019): test method for vickers indentation hardness of advanced ceramics, (2019) 10. https://doi.org/10.1520/C1327-15R19.
[55] E. Rocha-Rangel, Fracture toughness determinations by means of indentation Fracture. Nanocomposites with Unique Properties and Applications in Medicine and Industry, InTech, 2011, https://doi.org/10.5772/18127.
[56] G.R. Anstis, P. Chantikul, B.R. Lawn, D.B. Marshall, A critical evaluation of indentation techniques for measuring fracture toughness: I, direct crack measurements, J. Am. Ceram. Soc. 64 (1981) 533–538, https://doi.org/10.1111/j.1151-2916.1981.tb10320.x.
[57] G. Franceschin, R. Zanini, G. Iori, E. Longo, G. Divitini, G. Tromba, A. Traviglia, Non-destructive 3D exploration of silicate glass corrosion: a combined multiscale approach from the macro to the nanoscale, Phys. Chem. Chem. Phys. 26 (2024) 9697–9707, https://doi.org/10.1039/D3CP05221D.
[58] M. Achintha, A validated modelling technique for incorporating residual stresses in glass structural design, Structures 29 (2021) 446–457, https://doi.org/10.1016/j.istruc.2020.11.052.
[59] J.O. Isard, The mixed alkali effect in glass, J. Non. Cryst. Solids. 1 (1969) 235–261, https://doi.org/10.1016/0022-3093(69)90003-9.
[60] M. Melcher, R. Wiesinger, M. Schreiner, Degradation of glass artifacts: application of modern surface analytical techniques, Acc. Chem. Res. 43 (2010) 916–926, https://doi.org/10.1021/ar9002009.
[61] K. Damodaran, S. Gin, S. Narayanasamy, J.-M. Delaye, On the effect of Al on alumino-borosilicate glass chemical durability, Npj. Mater. Degrad. 7 (2023) 46, https://doi.org/10.1038/s41529-023-00364-3.
[62] A.K. VARSHNEYA, Influence of strain energy on kinetics of ion exchange in glass, J. Am. Ceram. Soc. 58 (1975) 106–109, https://doi.org/10.1111/j.1151-2916.1975.tb19569.x.
[63] A.E. Krauklis, A.I. Gagani, K. Vegere, I. Kalnina, M. Klavins, A.T. Echtermeyer, Dissolution kinetics of R-glass fibres: influence of water acidity, temperature, and stress corrosion, Fibers 7 (2019) 22, https://doi.org/10.3390/fib7030022.
[64] O. Schalm, G. Nuyts, K. Janssens, Some critical observations about the degradation of glass: the formation of lamellae explained, J. Non. Cryst. Solids. 569 (2021) 120984, https://doi.org/10.1016/j.jnoncrysol.2021.120984.
[65] U.J. Udi, M.M. Yussof, K. Musa Ayagi, C. Bedon, M. Khairul Kamarudin, Environmental degradation of structural glass systems: a review of experimental research and main influencing parameters, Ain. Shams Eng. J. 14 (2023) 101970, https://doi.org/10.1016/j.asej.2022.101970.
[66] G.W. Morey, R.O. Fournier, J.J. Rowe, The solubility of amorphous silica at 25°C, J. Geophys. Res. 69 (1964) 1995–2002, https://doi.org/10.1029/JZ069i010p01995.

[67] D.J. Belton, O. Deschaume, C.C. Perry, An overview of the fundamentals of the chemistry of silica with relevance to biosilicification and technological advances, FEBS. J. 279 (2012) 1710–1720, https://doi.org/10.1111/j.1742-4658.2012.08531.x.
[68] G.W. Scherer, Mechanics of syneresis I. Theory, J. Non. Cryst. Solids. 108 (1989) 18–27, https://doi.org/10.1016/0022-3093(89)90328-1.
[69] O. Majérus, P. Lehuédé, I. Biron, F. Alloteau, S. Narayanasamy, D. Caurant, Glass alteration in atmospheric conditions: crossing perspectives from cultural heritage, glass industry, and nuclear waste management, Npj. Mater. Degrad. 4 (2020) 27, https://doi.org/10.1038/s41529-020-00130-9.
[70] H. Sreenivasan, W. Cao, Y. Hu, Q. Xiao, M. Shakouri, M. Huttula, J.L. Provis, M. Illikainen, P. Kinnunen, Towards designing reactive glasses for alkali activation: understanding the origins of alkaline reactivity of Na-Mg aluminosilicate glasses, PLoS. One 15 (2020) e0244621, https://doi.org/10.1371/journal.pone.0244621.
[71] E.I. Kamitsos, A.P. Patsis, G. Kordas, Infrared-reflectance spectra of heat-treated sol-gel-derived silica, Phys. Rev. B 48 (1993) 12499–12505, https://doi.org/10.1103/PhysRevB.48.12499.
[72] J. McCloy, N. Washton, P. Gassman, J. Marcial, J. Weaver, R. Kukkadapu, Nepheline crystallization in boron-rich alumino-silicate glasses as investigated by multi-nuclear NMR, Raman, & Mössbauer spectroscopies, J. Non. Cryst. Solids. 409 (2015) 149–165, https://doi.org/10.1016/j.jnoncrysol.2014.11.013.
[73] A.K. Yadav, P. Singh, A review of the structures of oxide glasses by raman spectroscopy, RSC. Adv. 5 (2015) 67583–67609, https://doi.org/10.1039/C5RA13043C.
[74] T. Grammes, Structure and mechanical properties of aluminosilicate glasses. Doktor-Ingenieur (Dr.-Ing.), Friedrich-Schiller-Universität Jena, 2020.
[75] H. Liu, H. Kaya, Y. Lin, A. Ogrinc, S.H. Kim, Vibrational spectroscopy analysis of silica and silicate glass networks, J. Am. Ceram. Soc. 105 (2022) 2355–2384, https://doi.org/10.1111/jace.18206.
[76] K.E. Lipinska-Kalita, Infrared spectroscopic investigation of structure and crystallization of aluminosilicate glasses, J. Non. Cryst. Solids. 119 (1990) 310–317, https://doi.org/10.1016/0022-3093(90)90304-5.
[77] A. Aronne, S. Esposito, P. Pernice, Ftir and dta study of lanthanum aluminosilicate glasses, Mater. Chem. Phys. 51 (1997) 163–168, https://doi.org/10.1016/S0254-0584(97)80287-8.
[78] C. Huang, E.C. Behrman, Structure and properties of calcium aluminosilicate glasses, J. Non. Cryst. Solids. 128 (1991) 310–321, https://doi.org/10.1016/0022-3093(91)90468-L.
[79] N.J. Clayden, S. Esposito, A. Aronne, P. Pernice, Solid state 27Al NMR and FTIR study of lanthanum aluminosilicate glasses, J. Non. Cryst. Solids. 258 (1999) 11–19, https://doi.org/10.1016/S0022-3093(99)00555-4.
[80] C.I. Merzbacher, W.B. White, The structure of alkaline earth aluminosilicate glasses as determined by vibrational spectroscopy, J. Non. Cryst. Solids. 130 (1991) 18–34, https://doi.org/10.1016/0022-3093(91)90152-V.
[81] D.A. McKeown, F.L. Galeener, G.E. Brown, Raman studies of Al coordination in silica-rich sodium aluminosilicate glasses and some related minerals, J. Non. Cryst. Solids. 68 (1984) 361–378, https://doi.org/10.1016/0022-3093(84)90017-6.
[82] F. Wu, Y. Huang, H. Tao, P. Jiao, Z. Xiao, J. Jia, Sodium and potassium mixed effects on the viscoelastic behavior of silicate glasses, Materials 18 (2025) 1337, https://doi.org/10.3390/ma18061337.
[83] M. Okuno, N. Zotov, M. Schmücker, H. Schneider, Structure of SiO2–Al2O3 glasses: combined X-ray diffraction, IR and raman studies, J. Non. Cryst. Solids. 351 (2005) 1032–1038, https://doi.org/10.1016/j.jnoncrysol.2005.01.014.
[84] L. Bartlett, R. Gerald II, J. Huang, F. Mumtaz, R. O'Malley, T. Sander, J. Smith, H. Tekle, B. Zhang, The study of the behavior of CaO-SiO2-Al2O3-Na2O-based mold flux at 1400°C by a Fiber-optic raman sensor, in: AISTech 2023 Proceedings, AIST, 2023, pp. 1227–1237, https://doi.org/10.33313/387/135.
[85] J.M. Bennett, L. Mattsson, Introduction to Surface Roughness and Scattering, Optical Society of America, 1989.
[86] T. Kishii, Surface stress meters utilising the optical waveguide effect of chemically tempered glasses, Opt. Lasers. Eng. 4 (1983) 25–38, https://doi.org/10.1016/0143-8166(83)90004-0.
[87] T.M. Gross, H. Liu, Y. Zhai, L. Huang, J. Wu, The impact of densification on indentation fracture toughness measurements, J. Am. Ceram. Soc. 103 (2020) 3920–3929, https://doi.org/10.1111/jace.16793.
[88] A general mechanism for gel layer formation on borosilicate glass under aqueous corrosion, (n.d.). https://doi.org/10.1021/acs.jpcc.9b10491.s001.
[89] C.J. Brinker, G.W. Scherer, Sol-Gel Science : the Physics and Chemistry of Sol-Gel Processing, Elsevier Science, 2014.
[90] J.A.. Dean, N.A. Lange, Lange's Handbook of Chemistry, McGraw-Hill; [Distributed by] Knovel, 2001.